



**UIT**

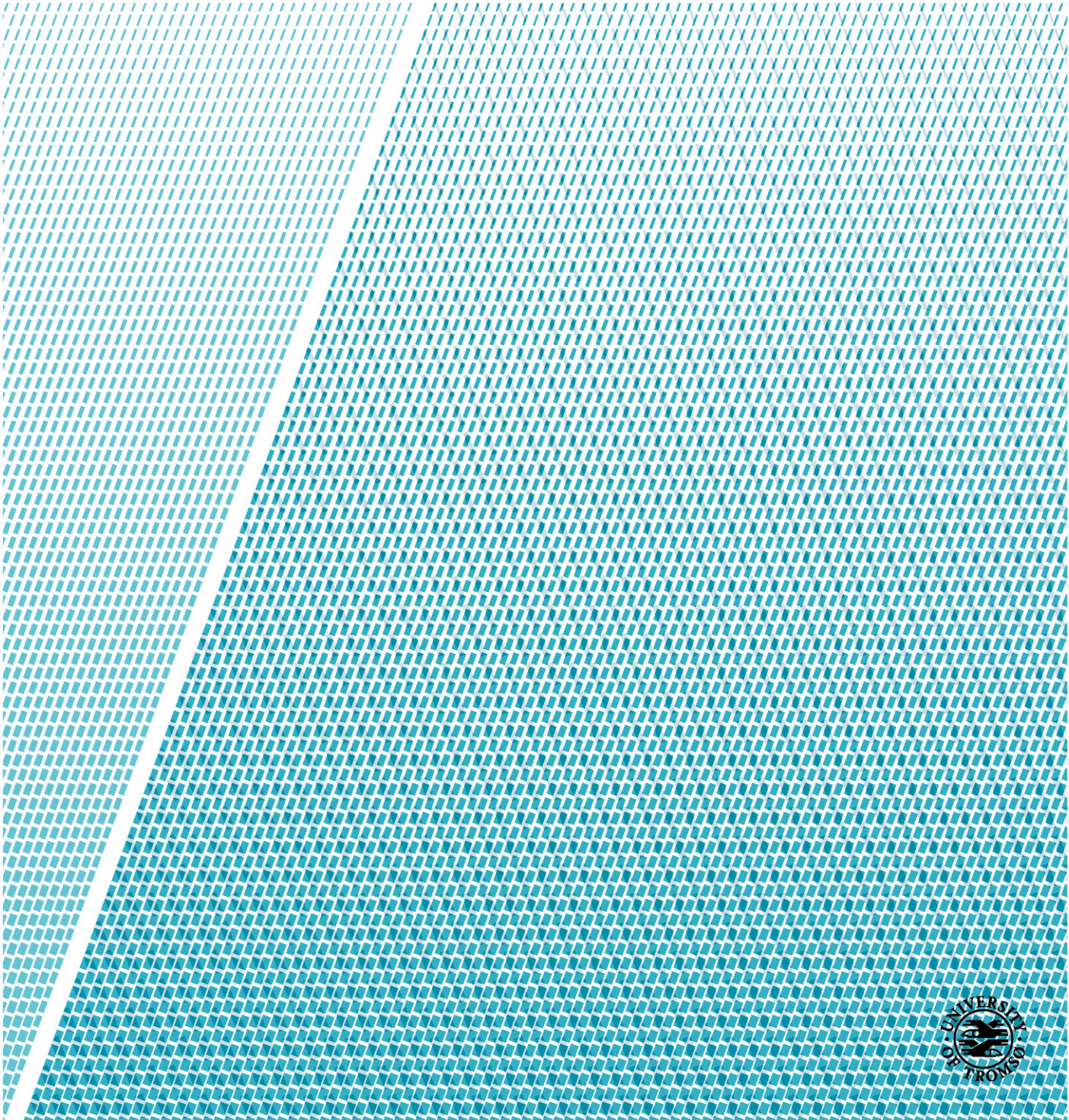
THE ARCTIC  
UNIVERSITY  
OF NORWAY

Faculty of Science and Technology  
Department of Physics and Technology

# **Coded Signals for High Frequency Ultrasound Imaging**

—  
**Chengxiang Peng**

*FYS-3900 Master Thesis in Physics — May 2019*





## Abstract

Degeneration of articular cartilage is known as a serious and painful knee disease seriously affecting people in all ages. The disease also marks the presence of osteoarthritis which is a complex musculoskeletal disorder. A successful assessment of the degeneration status is of great importance for estimating osteoarthritis progression, and thereby beneficial for implementing clinical treatments. Ultrasound has played a vital role in imaging the articular cartilage since it is capable of providing distinct information of important cartilage structures. However, various types of noise in ultrasound signals (e.g. clutter noise) are known to limit the quality of ultrasound images, especially at high frequencies where wave attenuation becomes severe. The possibility for improving the signal to noise ratio (SNR) by using coded signals is therefore the motivation behind this thesis, with the main objective is to investigate suitable codes and compression methods for cartilage imaging.

The main focus of this thesis has been put on coded ultrasound signals and related signal processing methods. Transducers made from two different piezoelectric materials (PZT and PVDF) are used to image a thick cartilage sample. For each transducer, three different waveforms (Ricker wavelet, Gaussian chirped, and a 13-bit Barker) are used to excite the ultrasonic transducers. Two different wave compression methods (Matched filtering and Wiener filtering) are also explored to decode the signals received by transducers. Ahead of processing the received signals, a time calibration was used to compensate for sample tilting, yielding an improved precision in the phase/time delay. A maximum method and a center of mass method were used for calibration.

The results from the experimental work show that both Chirp coded signals and Barker coded signals work well in improving the SNR, and that both transducers are able to produce high quality images of the cartilage sample. For the situations using coded excitation signals, however, the PZT transducer has high requirement for excitation repetition frequency because of its built-in delay line. Different time calibration methods have their own applicable conditions. Matched filter and Wiener filter both perform well for decoding, but the “noise” parameter in the Wiener filter has to be adjusted carefully to produce reasonable results.



## Acknowledgements

First, I would like to thank my supervisor, Frank Melandø. You have been a constant motivator and gave me excellent guidance during my master study. I have been lucky enough to have a supervisor who has highly professional dedication to science, and who always helped me to solve my questions and queries with patience. Your spirit of hard working and attitudes toward science make a real difference in the rest of my life.

I must express my gratitude to Anowarul Habib who helped me to design the experiments and gave me advice in writing. It has always been nice experience working with you.

There are also many others who have helped me during my study life at UIT. Your help, regardless of size, have all been priceless. Thanks to all of you sincerely.

*Chengxiang Peng*  
*Tromsø, May 2019*



# Contents

<b>Abstract</b>	<b>i</b>
<b>Acknowledgements</b>	<b>iii</b>
<b>List of Figures</b>	<b>vii</b>
<b>List of Tables</b>	<b>ix</b>
<b>1 Introduction</b>	<b>1</b>
1.1 Research background.....	1
1.1.1 Articular cartilage and its degeneration.....	1
1.1.2 Significance of ultrasound with coded excitation.....	3
1.2 Previous research.....	3
1.3 Structure of the thesis .....	4
<b>2 Acoustic theory</b>	<b>7</b>
2.1 Acoustic wave equation.....	7
2.1.1 Basic equations of fluid dynamics.....	7
2.1.2 Deriving wave equation.....	9
2.2 Acoustic impedance.....	11
2.3 Reflection and refraction .....	11
2.4 Attenuation .....	13
2.5 Ultrasonic transducer.....	15
2.5.1 Piezoelectric effect .....	15
2.5.2 Transducer frequency response .....	16
2.5.3 Backing and matching layer .....	17
2.5.4 Focused and unfocused transducers .....	17
<b>3 Ultrasound imaging and coded excitation</b>	<b>21</b>
3.1 Imaging principles .....	21
3.1.1 Pulse-echo technique.....	21
3.1.2 Time of flight method .....	21
3.1.3 Resolution .....	23
3.1.4 Noise.....	25
3.1.5 Imaging modes.....	25
3.2 Matched filter .....	26
3.3 Coded excitation.....	27
3.3.1 Basic principles .....	27
3.3.2 Evaluation criteria.....	29
3.3.3 Chirp excitation .....	30
3.3.4 Phase modulation and barker excitation .....	34

3.4	Mismatched filter.....	37
<b>4</b>	<b>Experiment implementation</b>	<b>39</b>
4.1	Experiment goals .....	39
4.2	Experiment flow .....	39
4.3	Equipment and cartilage sample.....	40
4.4	Data processing.....	42
4.4.1	Time calibration .....	42
4.4.2	Interpolation .....	44
4.4.3	Filtering .....	44
4.4.4	Image generation.....	45
<b>5</b>	<b>Results and discussion</b>	<b>47</b>
5.1	Discussion on excitation signals.....	47
5.2	Discussion on time calibration .....	49
5.3	Discussion on decoding methods .....	52
5.3.1	Discussion on filtering domain of Matched filter .....	52
5.3.2	Discussion on “noise” parameter of Wiener filter .....	53
5.3.3	Discussion on SNR, axial resolution and PSL.....	54
5.3.4	Discussion on templates.....	56
5.4	Discussion on PZT and PVDF transducers .....	56
5.5	Discussion on C scan and B scan images .....	57
<b>6</b>	<b>Main summary, conclusions and further work</b>	<b>63</b>
6.1	Main summary and conclusions .....	63
6.2	Further work .....	63
	<b>Bibliography</b>	<b>65</b>
	<b>Appendices</b>	<b>69</b>
<b>A</b>	<b>PZT transducer</b>	<b>71</b>
<b>B</b>	<b>PVDF transducer</b>	<b>73</b>

## List of Figures

1.1	Cross section of a typical synovial joint.....	2
1.2	Structural organization of articular cartilage.....	2
2.1	Control volume for Newton's second law.....	8
2.2	Control volume for conservation of mass.....	9
2.3	Waves propagate at normal incident.....	12
2.4	Waves propagate at oblique incident.....	13
2.5	Sources of acoustic energy losses.....	14
2.6	Piezoelectric material plated with metal.....	16
2.7	Transducer frequency response.....	16
2.8	Simple sketch of a transducer.....	17
2.9	Schematic of unfocused and focused beam.....	18
2.10	Simple sketch of a transducer.....	18
2.11	Graphic representation of parameters of focused beam.....	19
3.1	Sketch of ultrasound pulse echo system.....	21
3.2	Sketch of time location of pulse.....	22
3.3	Envelope extraction using Hilbert transform.....	23
3.4	Lateral resolution.....	24
3.5	Axial resolution.....	24
3.6	An example of B mode image showing human tissues.....	25
3.7	3D ultrasound reconstruction.....	26
3.8	Signal processing flow of a linear filter.....	26
3.9	Block diagram of coded ultrasound system.....	28
3.10	Basic principle of Coded excitation.....	28
3.11	Mainlobe and sidelobes of a compressed wave.....	29
3.12	Compressed wave.....	31
3.13	Signals and their spectrum.....	33
3.14	Barker code ( $N = 7$ ).....	36
3.15	Auto-correlation.....	37
4.1	Schematic overview of the ultrasonic scanning system.....	40
4.2	Schematic diagram of the experiment flow.....	40
4.3	Human cartilage sample.....	41
4.4	Scanning acoustic microscope.....	41
4.5	Schematic diagram of the PZT focused transducer.....	42
4.6	Cartilage sample.....	43
4.7	Time series of a pixel.....	43
4.8	Two signals collected from two positions.....	43
4.9	Schematic diagram of B scan, C scan and D scan.....	46
5.1	13-bit Barker coded signal used in experiment.....	47
5.2	Chirp coded signal and Ricker signal used in experiment.....	48
5.3	Spectrum of excitations.....	48

5.4	Signals before and after interpolation.....	49
5.5	Time calibration for case 1 .....	50
5.6	Results from center of mass method for case 1 .....	51
5.7	Time calibration for case 4 .....	52
5.8	Matched filtering both in time and frequency domain .....	53
5.9	Filtered signals of first scanning point .....	54
5.10	C scan images (PZT) .....	58
5.11	C scan images (PVDF) .....	59
5.12	B scan images (PZT) .....	60
5.13	B scan images (PVDF) .....	61

## List of Tables

2.1	Attenuation coefficients-typical values.....	15
3.1	Barker sequences .....	37
4.1	Different cases used in the experiment .....	40
4.2	Filtering situations .....	45
5.1	SNR, axial resolution and PSL .....	56



# Chapter 1

## Introduction

This thesis is a study of how to implement coded signals on a high frequency scanning acoustic microscope (SAM), and how to decode the received information. The decoding of the information received in terms of sampled time series, is also known as wave compression since the purpose is to compress a time series with long time extension into a short “delta”-like pulse. Prepared samples of articular cartilage have been used to evaluate the performance of several codes and compression methods.

With the increase of joint diseases and resulting reduction in life quality, the interest of doing research on articular cartilage has gradually heightened [1]. Osteoarthritis (OA) is the most common joint disease yielding substantial economic loss and morbidity [2]. An essential hallmark of OA is degradation of articular cartilage [3]. High frequency ultrasound has played an important role in imaging human articular cartilage which is quite helpful for determining the level of degeneration of human articular cartilage. In ultrasound imaging, signal to noise ratio (SNR) is a critical issue. However, it can be often difficult to meet the SNR required for high dynamical range and good resolution, especially when deep penetration is required. Coded signals are often employed in commercial medical imaging systems to increase SNR, which makes it possible to image deeper with acceptable dynamical range and resolution.

This chapter starts with a brief introduction of articular cartilage and significance of coded excitation. Then a short description of earlier research is presented. The last part of this chapter describes the structure of this thesis.

## 1.1 Research Background

### 1.1.1 Articular Cartilage and its degeneration

Cartilage is a very important body component providing connectivity and elastic support for a large number of body parts (e.g. bearing joints, air tubes, skin, nose, ears). The elasticity is provided by long fibers known as collagen which is categorized in three types (type I, II and III) [4]. Articular cartilage which refers to the cartilage in arthrodiar joints is a firm, elastic and flexible connective tissue with collagen fibers and cells known as chondrocytes, as important components. More specifically, this collagen lies on the surface of bones and contains no blood vessels or nerves [5] [6]. The main function of articular cartilage is to provide shock absorption from body forces and lubricated surface for joints. The latter function allows bones to slide over one another, thus reducing friction and increasing protection to damage brought by applied stress [7]. In human body, the thickness of articular cartilage varies from 1 to 7 mm relying on the location of the articular cartilage in the body [8]. Typically, articular cartilage is divided into four zones between the subchondral bone and articular surface which includes superficial zone, middle zone, deep zone and calcified zone [7]. Figure 1.1 presents a cross section of a typical synovial joint which includes cartilage. Figure 1.2 shows the structure of articular

cartilage.

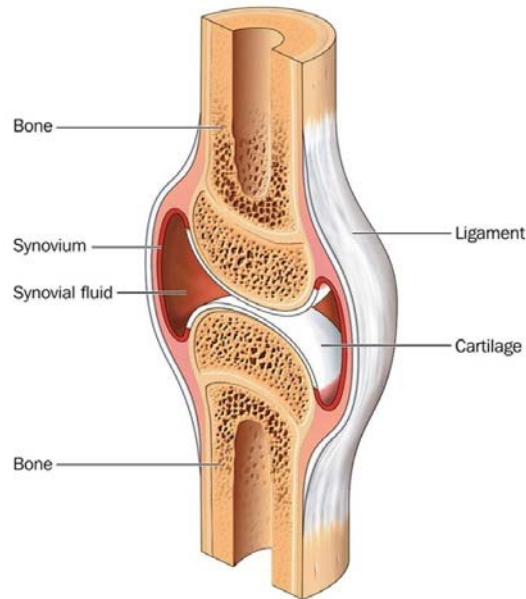


Figure 1.1: Cross section of a typical synovial joint [9]

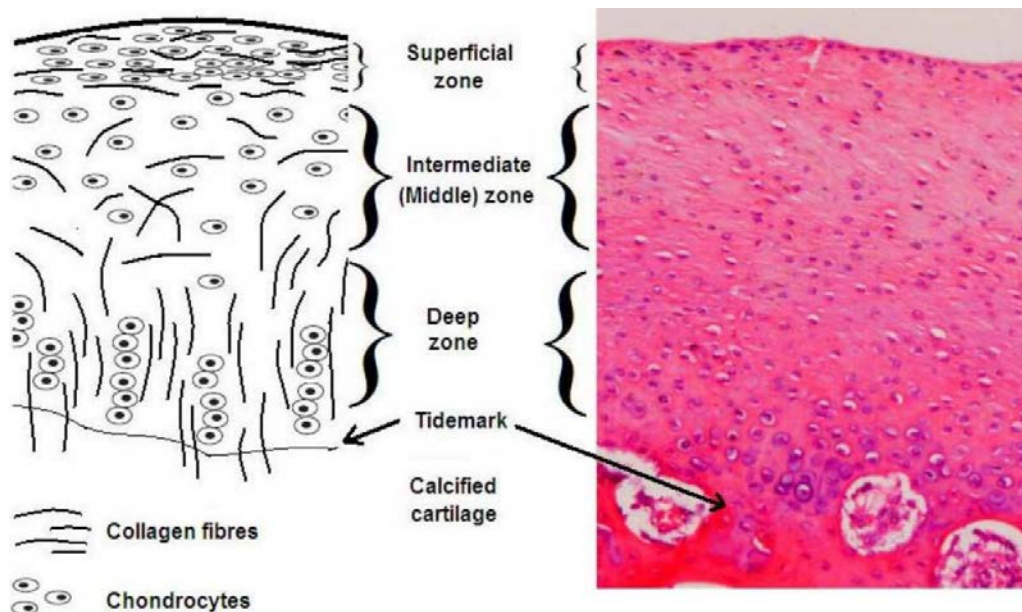


Figure 1.2: Structural organization of articular cartilage [8]

Cartilage degeneration is a type of complex musculoskeletal disorder which is mainly results from trauma, disease, heavy mechanical loading and aging. Depending on the level of degeneration, cartilage degeneration can be divided into three categories: superficial matrix disruption, partial thickness defects and full thickness defects [8]. For superficial matrix disruption, extracellular matrix is damaged and chondrocytes aggregate into clusters, while the matrix is able to self-repair. Partial thickness defects is a situation that the cartilage surface is disrupted but subchondral bone is not affected. Partial thickness defects cannot be repaired by the tissue itself. Full thickness defects disrupt both cartilage

surface and the subchondral bone [10]. Cartilage degeneration usually leads to loss of cartilage and then a presentation of osteoarthritis. Osteoarthritis is the most common form of joint diseases, resulting in pain and significant health care burden for millions of people worldwide.

### 1.1.2 Significance of ultrasound with coded excitation

Accurate assessment of cartilage degeneration is important for determining a suitable treatment. Ultrasound is an available and relatively inexpensive technique that has proved to be a reliable technique for screening articular cartilage in patients with OA [11]. In ultrasound imaging, image quality of ultrasound scanning system highly depends on resolution and penetration depth. Nevertheless, ultrasound signals are severely attenuated in human tissue, which results in low resolution and detection depth.

In conventional pulse-echo ultrasound imaging system, there is always a trade-off between resolution and penetration depth. Requirements of high resolution means short pulses normally are needed, which again will lower the total signal energy. Increasing the peak intensity level is often not an appropriate solution e.g. due to safety level for human tissue and cost issues for electronics and transducers. On the other hand, long waveforms containing more energy spread out over time will normally allow deeper imaging due to improved SNR, but at the price of lower resolution.

One known solution for obtaining high penetration depth without degrading imaging resolution, will be the so-called coded excitation. This method can improve the shortcoming of conventional ultrasound imaging system, and thereby potentially improve the diagnosis of many clinical diseases.

## 1.2 Previous research

Coded signals were first applied in radar system and were initially considered for use in the medical ultrasound system in 1979 by Takeuchi [12]. Takeuchi emphasized several benefits of using long excitation pulses spreading out the wave energy over time. It could for instance, increase the time-bandwidth product (TBP) to values much larger than 1, and therefore improve the SNR significantly compared to short pulse systems with TBP around 1. However, it was pointed out that long waveforms will induce unwanted sidelobes that severely affect imaging quality e.g. in terms reduced depth resolution. It was also mentioned that coded excitation ultrasound systems are much more complicated to implement than conventional pulse-echo ultrasound systems. Among the many challenges imposed by using long excitation sequences, it was shown that signals from long excitation sequences have to be coded in a special way in order to conserve the imaging quality and depth resolution.

In the earliest coded ultrasound systems, pseudo-random coded signal was used as excitation [13]. Pseudo-random coded signal did not show significant advantages compared with conventional single-pulse signal because of the high sidelobes produced by pseudo-random coded signal, therefore pseudo-random coded signal was abandoned

gradually.

Another popular and currently used approach is to use Chirp codes. Chirp coded signal is an analytical and easy approach to obtain a specified frequency characteristic which is widely used in the coded ultrasound systems. Investigators such as O' Donnell, Pollakowski and Misaridis have done extensively research on ultrasound systems excited by Chirp coded signals [14] [15] [16]. Another widely used approach is to use binary coded signals such as Golay codes and Barker codes. These codes are popular because the corresponding transmitting circuits and Matched filters are relatively simple. Golay coded signals was firstly considered to be used in ultrasound imaging system by Takeuchi [12]. Although Golay coded signals can be used to perfectly solve the sidelobes problem, they need to be transmitted two times. This means Golay coded signals are best suitable for ultrasound imaging system with low requirements for frame rates [17]. Compared with Golay coded signals, Barker coded signals only need to be transmitted one time. This means Barker coded signals are less affected by tissue motion and frame rate. Nowadays, one of the most frequently used single transmitted binary code is Barker code, although it has disadvantages in terms of sidelobes and available code lengths (maximum 13 bits).

In addition to works on signal coding, many publications can also be found on wave compression methods and pre-distorted coded signals. Some researchers have considered the application of Mismatched filters such as inverse filter and Wiener filter for more reduction of sidelobes [18] [19]. Behar and Raman discussed the design of pre-distorted coded signals to improve axial resolution [20] [21].

### **1.3 Structure of the thesis**

By means of experiment designing and data analysis, this thesis investigates coded signals and related wave compression methods for cartilage imaging done by a high frequency scanning acoustic microscope. The basic knowledge of acoustic and theoretical part of coded signals and wave compression methods are discussed in the first part of this thesis. The second part is mainly devoted to experimental description and data analyzing. The specific structure of this thesis is as follows:

Chapter 1 gives a brief introduction on the research background, significance of ultrasound with coded excitation, previous research and structure of this thesis.

Chapter 2 presents basic principles of acoustic theory, including wave propagation and ultrasonic transducer.

Chapter 3 describes ultrasound imaging principles, coded signals and wave compression methods. Emphasis is given on coding and decoding.

Chapter 4 gives a description of the implementation of experiment.

Chapter 5 presents and discusses experimental results of coded excitation in cartilage imaging. Emphasis is given on performance analysis of coded excitations and data processing methods.

Chapter 6 summarizes the thesis and gives suggestions for future work.



## Chapter 2

### Acoustic theory

Imaging and signal processing of acoustic data are both basic tools needed to extract information from the ultrasound waves. For an efficient use of these tools it is essential to understand the wave physics of ultrasound. An ultrasound transducer is the device that normally is used to produce the ultrasonic waves, and to receive the backscatter that is produced from the investigated target. Therefore, it is important to have a general understanding of ultrasound transducer. Properties of acoustic waves with different wavelengths are normally quite similar unless one goes to extreme limits, meaning that we do not need to pay special attention to waves in the ultrasonic regime. This chapter starts with the description of the basic acoustic theory. And then a brief introduction of ultrasound transducer is presented. The complete theory on which this chapter is based can be found in Refs. [22] [23] and [24].

#### 2.1 Acoustic wave equation

##### 2.1.1 Basic equations of fluid dynamics

Sound is a pressure disturbance which needs a media to propagate. During its propagating, the pressure depends both on the location and time. The wave equation is used to describe the relations among pressure, location and time. Fluid is one of the most general media in which ultrasound propagates. The wave equation is derived under the circumstance of propagating in ideal fluid.

Three basic equations are needed to derive the wave equation of acoustics. The three basic equations are derived from three basic principles which are named as conservation of mass, Newton's second law and equation of state. To simplify the derivation, some assumptions are made. Note that these assumptions do not influence the generality of wave equations.

These assumptions are:

1. The fluid is ideal which means the fluid is not viscous. Therefore, there is no energy loss when sound is propagating in this type of fluid.
2. The velocity of the fluid is zero when there is no disturbance.
3. The fluid is isotropic which means the pressure and density are all constants when there is no disturbance.
4. The amplitude of the disturbance is quite small. Acoustic pressure is quite small compared to the background pressure. Particle velocity is much smaller than the

sound velocity. Displacement of particle is much smaller than the wavelength.

Forces acting on a small control volume are analyzed based on the Newton's second law. The control volume is shown in Figure 2.1.

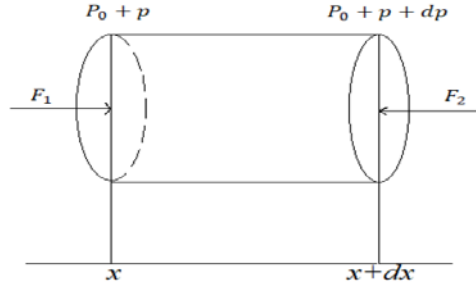


Figure 2.1: Control volume for Newton's second law

$S$  is the side area of the volume.  $dx$  is the length of the volume.  $p$  is sound pressure.  $P_0$  is background pressure.  $x$  is the coordinate.  $F_1$  is the force acting on the left side of the volume.  $F_2$  is the force acting on the right side of the volume.  $t$  is time.  $\rho$  is density of the media. Since the forces acting on different sides of the volume are different, the particles inside the volume will move. Some relations of those parameters are

$$F_1 = (P_0 + p)S, \quad (2.1)$$

$$F_2 = (P_0 + p + dp)S, \quad (2.2)$$

$$dp = \frac{\partial p}{\partial x} dx. \quad (2.3)$$

According to Newton's second law, the first basic equation can be written as

$$\rho S dx \frac{dv}{dt} = - \frac{\partial p}{\partial x} S dx. \quad (2.4)$$

After simplification, it is written as

$$\rho \frac{dv}{dt} = - \frac{\partial p}{\partial x}. \quad (2.5)$$

This equation describes the relation between acoustic pressure and particle velocity.

For the same control volume, the variation of mass should be equal to the difference of the mass flowing in and the mass flowing out in a unit time according to the conservation of mass, as shown in Figure 2.2.

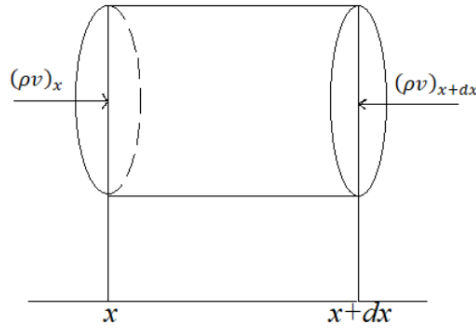


Figure 2.2: Control volume for conservation of mass

The mass flowing in is  $(\rho v)_x S$ . The mass flowing out is  $-(\rho v)_{x+dx} S$  which can be represented as  $-\left[(\rho v)_x + \frac{\partial(\rho v)_x}{\partial x} dx\right] S$  based on Taylor's formula. Therefore, the following equation can be used to express the conservation of mass for the control volume.

$$-\frac{\partial(\rho v)}{\partial x} S dx = \frac{\partial \rho}{\partial t} S dx. \quad (2.6)$$

After simplification, it is written as

$$-\frac{\partial(\rho v)}{\partial x} = \frac{\partial \rho}{\partial t}. \quad (2.7)$$

The above equation describes the relation between the particle velocity and media density.

Equation of state expresses the relation among thermodynamics parameters. When sound propagates in the control volume, the temperature, pressure and density will change. Pressure can be viewed as a function of density since we have assumed that sound propagating is an adiabatic process. The function can be written as

$$P = P(\rho). \quad (2.8)$$

The derivative of  $P$  is

$$dP = \left(\frac{dP}{d\rho}\right)_s d\rho. \quad (2.9)$$

The subscript  $s$  represents that the process is insulated. Considering that the changes of pressure and density are in the same direction,  $\left(\frac{dP}{d\rho}\right)_s$  is always above zero. Let  $\left(\frac{dP}{d\rho}\right)_s = c^2$ , here  $c$  is regarded as a coefficient temporarily. Equation (2.9) can be rewritten as

$$dP = c^2 d\rho. \quad (2.10)$$

### 2.1.2 Deriving wave equation

From the basic equations in the previous section, we can obtain the wave equation for

ideal fluid. With the help of assumptions, equation of momentum and conservation of mass can be rewritten as

$$\rho_0 \frac{\partial v}{\partial t} = -\frac{\partial p}{\partial x'} \quad (2.11)$$

$$-\rho_0 \frac{\partial v}{\partial x} = \frac{\partial \rho'}{\partial t}. \quad (2.12)$$

Where  $\rho_0$  is the media density in the equilibrium state and  $\rho'$  is the variation of density under oscillated state.

For pressure  $P$ , a Taylor's expansion in the neighborhood of equilibrium state is written as

$$P = P(\rho_0) + (\rho - \rho_0) \left( \frac{dP}{d\rho} \right)_{s,\rho_0} + \frac{1}{2} (\rho - \rho_0)^2 \left( \frac{d^2P}{d\rho^2} \right)_{s,\rho_0} + \dots \quad (2.13)$$

After arrangements, we have

$$\left( \frac{dP}{d\rho} \right)_s = \left( \frac{dP}{d\rho} \right)_{s,\rho_0} + \frac{1}{2} (\rho - \rho_0) \left( \frac{d^2P}{d\rho^2} \right)_{s,\rho_0} + \dots \quad (2.14)$$

Only the first term need be retained since the second term is quite small. Let  $\left( \frac{dP}{d\rho} \right)_{s,\rho_0} = c_0^2$ , we have the simplified equation of state

$$p = c_0^2 \rho'. \quad (2.15)$$

For small amplitude sound waves, three linear equations (2.11), (2.12) and (2.15) have been obtained so far. Based on the three equations, we can obtain the expression for acoustic pressure which only depends on time and location. Combining Eq. (2.11) and Eq. (2.12) we can have

$$\rho_0 c_0^2 \frac{\partial v}{\partial x} = -\frac{\partial p}{\partial t}. \quad (2.16)$$

By deriving Eq. (2.16) we can have

$$\rho_0 c_0^2 \frac{\partial^2 v}{\partial t \partial x} = -\frac{\partial p^2}{\partial t^2}. \quad (2.17)$$

By plugging Eq. (2.17) into Eq. (2.15), we finally get the wave equation

$$\frac{1}{c_0^2} \frac{\partial^2 p}{\partial t^2} = \frac{\partial p^2}{\partial x^2}. \quad (2.18)$$

Note that Eq. (2.18) is one-dimensional, and the three-dimensional wave equation can be similarly written as

$$\frac{1}{c_0^2} \frac{\partial^2 p}{\partial t^2} = \nabla^2 p. \quad (2.19)$$

Where  $\nabla^2$  is the Laplace operator. Its definition varies in various coordinate systems. Its definition in Cartesian coordinate system is

$$\nabla^2 = \frac{\partial^2 p}{\partial x^2} + \frac{\partial^2 p}{\partial y^2} + \frac{\partial^2 p}{\partial z^2}. \quad (2.20)$$

In terms of the solving the wave equation, Fourier transform method, separation of variables and d'Alembert's formula are the most general methods [25]. A standard form of solution is

$$p(x, t) = Ae^{j(\omega t - kx)}, \quad (2.21)$$

where  $A$  represents the amplitude of sound pressure,  $w$  stands for the angular frequency and  $k$  is the wave number. Note that Eq. (2.21) shows that the wave only propagates in the increasing  $x$  direction. The dispersion relation for Eq. (2.21) is

$$\omega = ck. \quad (2.22)$$

## 2.2 Acoustic impedance

Acoustic impedance is a key physical parameter when discussing sound propagation. It is because of acoustic impedance mismatch at the interface of two media, that sound reflection appears. This allows visualization with ultrasound [26]. Acoustic impedance can be generally regarded as the resistant ability a media has when the sound is propagating through it. Acoustic impedance  $Z$  is defined as

$$Z = \frac{p}{v}. \quad (2.23)$$

Another way to define acoustic impedance is

$$Z = \rho c. \quad (2.24)$$

Note that  $Z$  is a fixed constant for the media at specific conditions. Sound propagation is influenced more by  $Z$  than the separate  $\rho$  or  $c$ . When the temperature changes, the impedance also changes. If we use the terminology in circuit system to describe the sound propagation, acoustic impedance can be viewed as electrical impedance. Sound pressure can be viewed as voltage and particle velocity can be viewed as the current.

## 2.3 Reflection and refraction

Reflection and refraction are important physical properties which are explored in ultrasound and its applications. In ultrasound imaging and ultrasound diagnostics, reflection technology is widely used. Reflection technology is based on the pulse that is reflected from various media with different acoustic impedance [27]. This section presents the basic theory of sound reflection and refraction. The basic case is that the sound is hitting a large and flat boundary between two media perpendicularly.

The figure below shows how sound propagates between two media *I* and *II*. The particle velocity of incoming wave is  $v_i$ , and the particle velocity of reflected wave is  $v_r$ . The particle velocity of transmitted wave is  $v_t$ . The particle velocity at the interface near medium *I* is  $v_1$ , and the particle velocity at the interface near medium *II* is  $v_2$ . The pressure caused by incoming wave is  $p_i$ , and the pressure caused by reflected wave is  $p_r$ . The pressure caused by transmitted wave is  $p_t$ . The pressure at the interface near medium *I* is  $p_1$ , and the pressure at the interface near medium *II* is  $p_2$ . The acoustic impedance of medium *I* is  $Z_1$ , and the acoustic impedance of medium *II* is  $Z_2$ . The interface is at position  $x = 0$ .

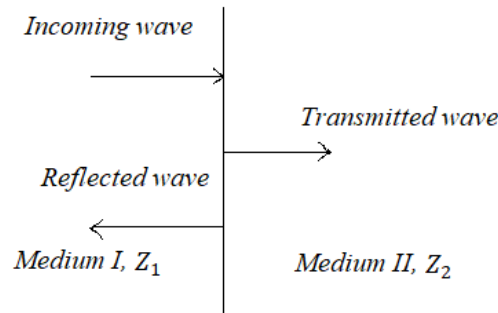


Figure 2.3: Waves propagate at normal incident

We now should specify a set of conditions that should be fulfilled at the interface between the two media. These conditions are:

1. Acoustic pressure is same on two sides of the boundary between two media.
2. Particle velocity is equal on two sides of the interface between two media.

The conditions can be written as

$$v_1 = v_2, \quad (2.25)$$

$$p_1 = p_2. \quad (2.26)$$

Then we get the following equations according to equations (2.25) and (2.26).

$$v_i + v_r = v_t, \quad (2.27)$$

$$p_i + p_r = p_t. \quad (2.28)$$

Combining equations (2.21), (2.23), (2.24), (2.27) and (2.28), we get the following equations

$$\frac{p_i}{Z_1} - \frac{p_r}{Z_1} = \frac{p_t}{Z_2}, \quad (2.29)$$

$$R_v = \frac{v_r}{v_i} = \frac{Z_1 - Z_2}{Z_2 + Z_1}, \quad (2.30)$$

$$T_v = \frac{v_t}{v_i} = \frac{2Z_1}{Z_2 + Z_1}. \quad (2.31)$$

Here  $R_v$  and  $T_v$  denote the reflection and transmission coefficients in terms of particle velocity. For the coefficients in terms of acoustic pressure, we have the equations

$$R_p = \frac{Z_2 - Z_1}{Z_2 + Z_1}, \quad (2.32)$$

$$T_p = \frac{2Z_2}{Z_2 + Z_1}. \quad (2.33)$$

The reflection and transmission coefficients are dominated by the acoustic impedance of media, which shows that the acoustics impedance has a great influence on sound propagation.

When a sound wave meets a boundary at oblique incidence, both reflection and refraction occur. This is shown in Figure 2.4. The incident angle is  $\theta_i$  that is equal to the reflection angle  $\theta_r$ . The refraction angle is  $\theta_t$ . The reflection and transmission coefficients in terms of pressure are

$$R_p = \frac{p_2 c_2 \cos \theta_i - p_1 c_1 \cos \theta_t}{p_2 c_2 \cos \theta_i + p_1 c_1 \cos \theta_t}, \quad (2.34)$$

$$T_p = \frac{2p_2 c_2 \cos \theta_i}{p_2 c_2 \cos \theta_i + p_1 c_1 \cos \theta_t}. \quad (2.35)$$

Where  $c_1$  is sound velocity in medium *I* and  $c_2$  is sound velocity in medium *II*.

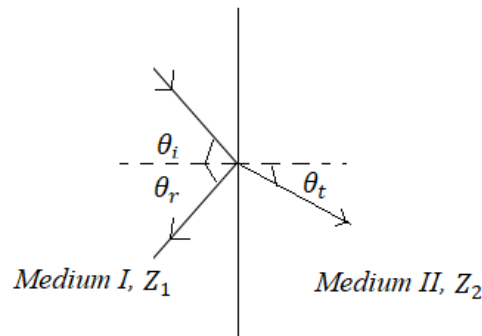


Figure 2.4: Waves propagate at oblique incident

## 2.4 Attenuation

Sound waves encounter losses when propagate in real media. Attenuation refers to the

losses in acoustic energy as the wave propagates in the media. There are several processes can lead to attenuation such as absorption, reflection, refraction and scattering. Figure 2.5 shows the processes.

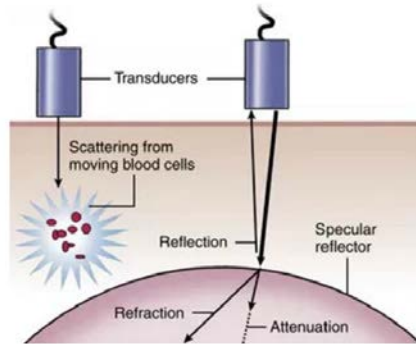


Figure 2.5: Sources of losses [28]

Ultrasound pressure and particle velocity reduce exponentially due to attenuation, according to

$$P = P_0 e^{-\alpha d}, \quad (2.36)$$

$$v = v_0 e^{-\alpha d}. \quad (2.37)$$

Where  $\alpha$  is attenuation coefficient. Then the beam intensity defined by  $I = Pv$  reduces as

$$I = I_0 e^{-2\alpha d}. \quad (2.38)$$

Where  $(\dots)_0$  denotes the initial values. We can see that the beam intensity attenuated more than sound pressure and particle velocity. To measure the attenuation, pressure at two positions are needed.

$$P_1 = P_0 e^{-\alpha d_1}, \quad (2.39)$$

$$P_2 = P_0 e^{-\alpha d_2}. \quad (2.40)$$

Where  $P_1$  is the pressure at position 1,  $d_1$  is the distance between position 1 and the initial position.  $P_2$  is the pressure at position 2,  $d_2$  is the distance between position 2 and the initial position. Then take the ratio between the measurements

$$\frac{P_2}{P_1} = e^{-\alpha(d_2 - d_1)}. \quad (2.41)$$

Then solve with respect to  $\alpha$ :

$$\alpha = \frac{20 \log_{10} \left( \frac{P_2}{P_1} \right)}{(d_1 - d_2) 20 \log_{10}(e)} \approx \frac{\left( \frac{P_2}{P_1} \right)_{dB}}{8.686(d_1 - d_2)}. \quad (2.42)$$

The attenuation is frequency dependent. And it can be estimated by

$$\alpha(f) = \alpha_0 + \alpha_1|f|^y. \quad (2.43)$$

Where  $f$  is the wave frequency.  $\alpha_0$ ,  $\alpha_1$  and  $y$  are all coefficients. Attenuation limits the penetration depth of sound in human body. The higher the frequency, the more the attenuation. Therefore, low frequency ultrasound usually used to image the tissue at large depth and vice versa. The dependence of frequency is linear or almost linear for most soft tissues. The frequency dependence is nonlinear for blood and tissues such as lung [29]. Some typical attenuation coefficients are listed in Table 2.1.

Tissue	Attenuation coefficients (1 MHz Beam, dB/cm)
Water	0.0002
Blood	0.18
Liver	0.4 – 0.7
Fat	0.5 – 1.8
Muscle	0.2 – 0.6
Bone	13 – 26
Lung	40

Table 2.1: Attenuation coefficients-typical values

## 2.5 Ultrasonic transducer

### 2.5.1 Piezoelectric effect

Transducer is a device that transforms energy from one type to another. The ultrasonic transducer is the fundamental component for sending and receiving ultrasonic waves. There are several types of ways to excite and detect the ultrasonic waves. The most commonly used is piezoelectric effect. The transducer using piezoelectric effect is piezoelectric transducer.

Piezoelectric effect refers to the phenomenon of some materials to generate an electric charge in response to application of mechanical stress. The piezoelectric effect is also reversible, meaning that the piezoelectric materials will change shape if electric current is applied to them. Some of the most widely used piezoelectric materials are quartz, lead zirconate titanate (PZT) and polyvinylidene fluoride (PVDF). To briefly show the physics of piezoelectric effect, the following equations are required.

$$D = D(E, S), \quad (2.44)$$

$$T = T(S, E). \quad (2.45)$$

Where  $D$  is electric displacements,  $E$  is electric field,  $T$  denotes stress and  $S$  denotes strain. For the above equation, the assumption is the system dimension should be much less than the electromagnetic wavelength. Usually conductive metal is placed on two opposite sides of the piezoelectric material, as is shown in Figure 2.6.

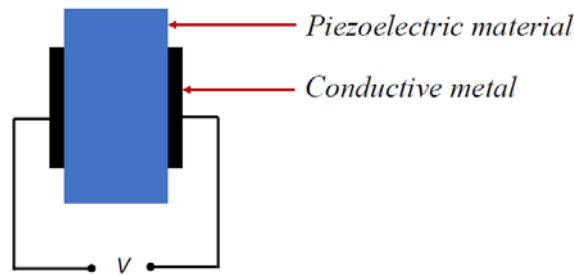


Figure 2.6: Piezoelectric material plated with metal

## 2.5.2 Transducer frequency response

Frequency response is a measure of output signal spectrum of a device in response to spectrum of input signal, and is used to describe the frequency characteristics of the device. Transducer frequency response is an important performance parameter for ultrasonic transducer. For pulse-echo ultrasound system, the bandwidth of the frequency response depends on the pulse length. As is shown in Figure 2.7, long spatial pulse length corresponds to a narrow bandwidth and vice versa.  $f_0$  is center frequency which depends on the resonance frequency of the transducer. The transducer bandwidth is mainly determined by wave damping induced by the backing material and the wave emission through the matching layers.

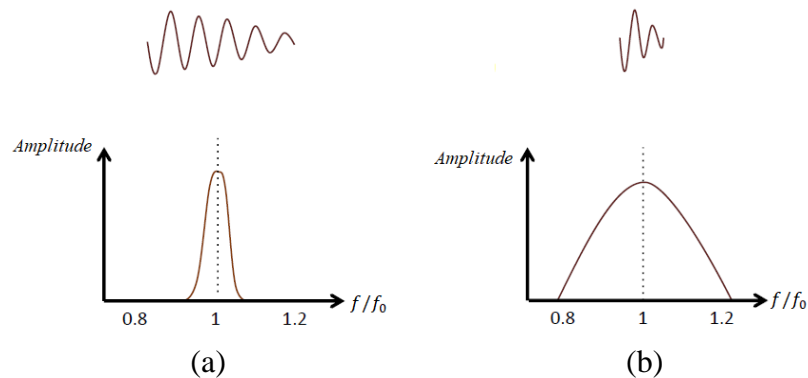


Figure 2.7: Pulse and frequency response. (a) Long pulse. (b) Short pulse

Transducer frequency response can be described by the so-called quality factor. As shown in Eq. (2.46), quality factor is defined by the ratio of center frequency to bandwidth. Low quality factor means wide bandwidth and high damping [30]. A transducer with high quality factor is good for continuous wave. For pulse echo imaging, a transducer with low quality factor is favorable.

$$Q = \frac{f_0}{BDF}. \quad (2.46)$$

Where  $Q$  is the quality factor,  $BDF$  is the bandwidth. Usually the upper and lower frequencies of the bandwidth are the frequencies whose corresponding amplitudes divided by peak amplitude is  $-3dB$ .

### 2.5.3 Backing and matching layers

A sketch of a typical signal element transducer is shown below.

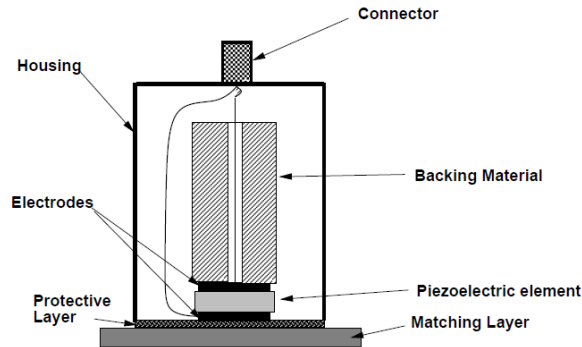


Figure 2.8: Simple sketch of a transducer [31]

There are matching and backing layers in front and back of the piezoelectric element. When the piezoelectric element is excited, it usually generates sound waves in both forward direction and backward direction. Generally, the wave propagating in backward direction is not desirable. The backward wave will be reflected to forward and then leads to increase of emitted pulse length, and therefore a more complicated interpretation of received signals is required. The backing layer is used to absorb the backward wave so that the reflected wave from it is highly attenuated. The acoustic impedance of the backing material should be almost equal to that of the transducer, and the backing material should also have a high attenuation coefficient.

The matching layer is used to bridge the acoustic impedance mismatch between the piezoelectric element and the target [32]. Because the acoustic impedance between the piezoelectric material and the target is quite different, ultrasonic wave will be reflected with a high amplitude at the interface. This is undesirable since we hope the wave can propagate in the target and then bring back the information of the target. To make sure that the ultrasound wave can propagate in the target efficiently, an intermediate material called matching layer is needed. The simplest way to find an appropriate acoustic impedance of the matching layer is

$$Z_m = \sqrt{Z_p Z_t}, \quad (2.47)$$

where  $Z_m$  is the acoustic impedance of the matching layer,  $Z_p$  is the acoustic impedance of the piezoelectric element and  $Z_t$  is the acoustic impedance of the target.

### 2.5.4 Focused and unfocused transducers

There are several types of ultrasound transducers in practical use such as linear array transducer, single-element transducer and etc. In this thesis, only single-element transducers are used, so only single-element transducers are discussed here. Single-element transducers can be grouped into focused and unfocused transducers according to the ultrasound beam geometry. As the name indicates, unfocused transducer emits the

unfocused beam and the focused beam is emitted by the focused transducer. Figure 2.9 shows the beam generated by the unfocused and focused transducer.

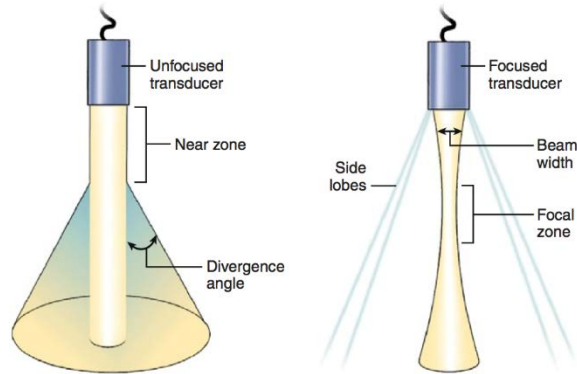


Figure 2.9: Schematic of unfocused and focused beam [28]

For unfocused transducer, the ultrasound beam can be broken into two distinct areas, the near zone and the far zone. The length of the near zone is approximately

$$N = \frac{D^2}{4\lambda}, \quad (2.48)$$

where  $N$  is length,  $D$  is the diameter of the transducer element and  $\lambda = \frac{c}{f}$ .  $f$  is the nominal frequency of the transducer. In the far zone the beam diverges with an angle  $\theta$  given by

$$\sin \theta \approx 1.22 \frac{\lambda}{D}. \quad (2.49)$$

By using a curved piezoelectric element or a flat piezoelectric element, a focused transducer can be obtained. The degree of focusing can be measured in terms of the so-called f-number which is defined as

$$F_N = \frac{F}{D}. \quad (2.50)$$

Here  $F_N$  is f-number and  $F$  is the focal distance, as is shown in the figure below.

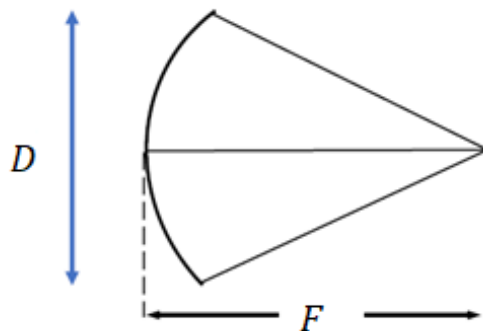


Figure 2.10: Simple sketch of focused distance and aperture diameter

There are several important parameters to describe the characteristics of the focused beam generated by the focused transducer. A graphic representation of the parameters is shown in Figure 2.11.

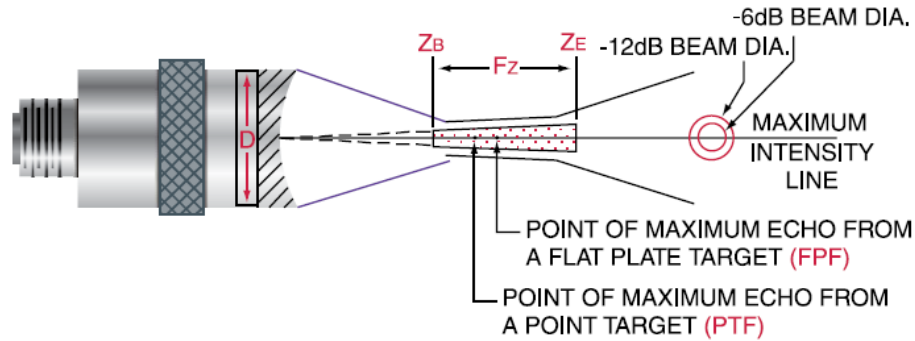


Figure 2.11: Graphic representation of parameters of focused beam [33]

In the above figure,  $F_Z$  is the focal zone,  $Z_B$  and  $Z_E$  are the starting and ending of the focal zone respectively. The locations of starting and ending points of the focal zone are places on which the on-axis beam intensity decreases to -6 dB of the intensity at the focal point. The depth of the field, namely  $F_Z$ , is

$$F_Z = Z_E - Z_B. \quad (2.51)$$

The approximate -6 dB beam diameter  $BD$  is

$$BD \approx \frac{1.028\lambda F}{D}, \quad (2.52)$$

Beam diameter is an important parameter since it affects the resolution of ultrasound image. More about imaging resolution will be discussed in next chapter. It is evident that beam diameter varies according to the distance to transducer. Normally the imaging target should be put on the focal point where the beam diameter is the narrowest.



## Chapter 3

### Ultrasound imaging and coded excitation

Due to the properties of ultrasound such as good directivity and small wavelength, ultrasound is widely used for imaging. Unlike X-ray, there is no ionizing radiation exposure associated with ultrasound. Ultrasound is generally considered safe, so it has been widely used in medical imaging for many years. One important issue in ultrasound imaging is noise reduction. Matched filter plays an important role in reducing random noise. To further improve the signal to noise ratio, coded excitation is employed. Mismatched filtering may behave better than Matched filtering when both random noise and speckle noise occur. Both Matched and Mismatched filtering can be used in pulse compression to keep the resolution.

This chapter begins with the description of the ultrasound imaging. Matched filtering and coded excitation are presented in the following part. In terms of coded signals, Barker code and Chirp code are illustrated. Mismatched filtering is presented in the last part.

#### 3.1 Imaging principles

##### 3.1.1 Pulse echo technique

Before the end of World War II, pulse echo technique was mainly used in the field of military and industry, such as radar and sonar. After World War II, pulse echo technique has been widely used in medical ultrasound especially in medical ultrasound imaging. Ultrasound pulses are emitted toward the objects by the ultrasonic transducer, which generate the reflected or scattered signals when encountering the tissue interface. The reflected or scattered signals are the so-called pulse echo signals. Pulse echo technique takes advantages of the pulse echo signals to form the images of the objects. A sketch of conventional ultrasound pulse echo system is shown below.

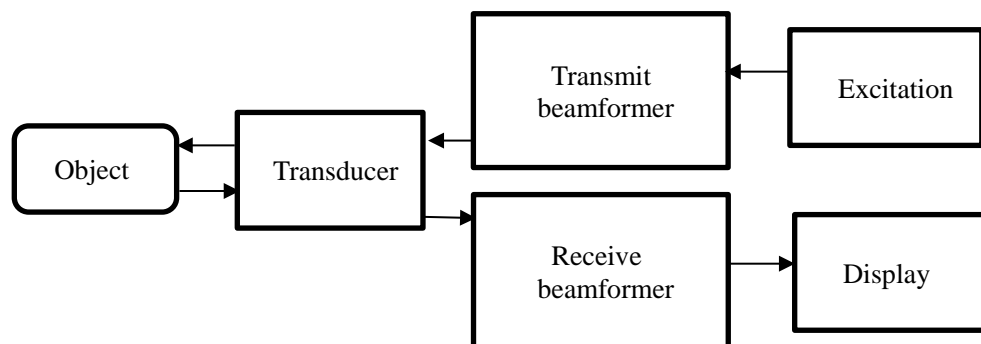


Figure 3.1: Sketch of ultrasound pulse echo system

##### 3.1.2 Time of flight methods

Ultrasound imaging is usually based on distance measurements. An ultrasound pulse echo signal is a time series, so what is really measured is the time difference between the emitted signal and the received echo signal. There are several ultrasonic distance measurements, the operating principle is measuring the pulse *time of flight* (TOF) [34] [35]. The transducer outputs a short pulse and receives an echo pulse. The distance can be calculated by the formula

$$d = \frac{cT_f}{2}, \quad (3.1)$$

where  $d$  is the distance,  $c$  is the velocity of sound and  $T_f$  is the time difference. From the above formula we can see that  $d$  depends on sound velocity and time difference. The distance uncertainly therefore originates from the estimation of the sound velocity and time difference. Sound velocity may not be constant when propagating in the media because the physical parameters or temperature may vary [36]. However, the velocity is often viewed as a constant in practical ultrasound imaging. In this case an accurate estimation of  $T_f$  is quite essential.

To estimate  $T_f$ , time location of echo signal need to be measured. Maximum amplitude method, center of mass method and Matched filter method are often employed to measure the time location of the echo signal. A sketch of time location of pulse is shown below. Where  $T_C$  is the time location of the pulse.

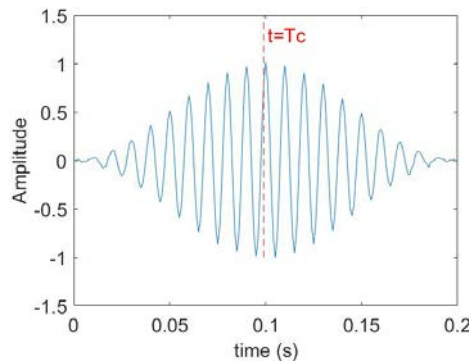


Figure 3.2: Sketch of time location of pulse

No matter which method is chosen, envelope estimating typically need to be applied in advance. Hilbert transform is one of the most widely used method to find the envelope of signals. In practical application, an analytical signal is generated according to Hilbert transform. The absolute value of the analytical signal is represented as the envelope [37]. Hilbert transform is defined as

$$H[r(t)] = \frac{1}{\pi} \int_{-\infty}^{+\infty} \frac{r(\tau)}{t - \tau} d\tau, \quad (3.2)$$

where  $t$  is time,  $r(t)$  is the echo pulse, and  $H[r(t)]$  is the Hilbert transform of the echo pulse. The analytical signal is

$$A[r(t)] = r(t) + j * H[r(t)]. \quad (3.3)$$

An example of envelope extraction using Hilbert transform is shown below.

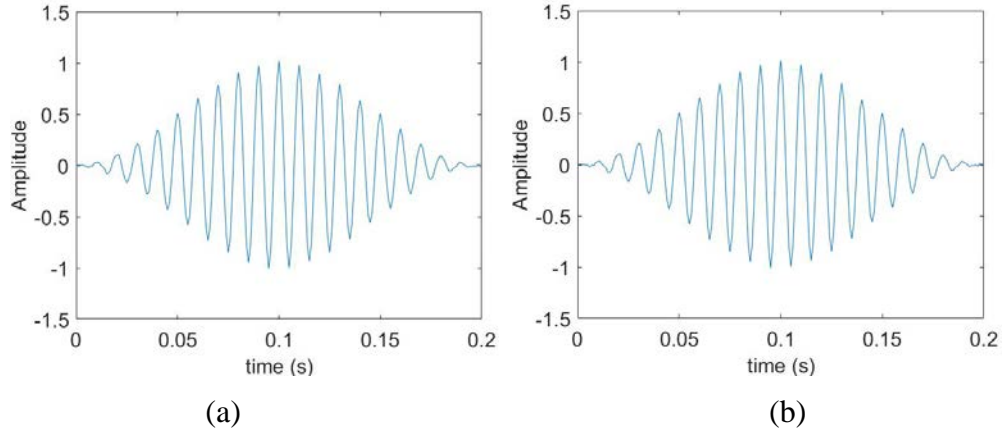


Figure 3.3: Envelope extracting using Hilbert transform. (a) Pulse. (b) Envelope

After the envelope has been extracted, time location of the echo pulse should be estimated. Maximum amplitude method uses  $T_C = T_m$  as the time location, where  $T_m$  is the time sample where the corresponding amplitude obtains the maximum value. This method is easy to implement but may gain large uncertainty.

Center of mass method uses all the sampling points of the pulse to estimate the time location. The level of uncertainty is lower than the maximum amplitude method while it is more complicated to implement. Consider  $a_i$  as the amplitude of the time point  $t_i$ , the estimated time location of the pulse is given by

$$T_C = \frac{\sum_{i=1}^N t_i a_i}{\sum_{i=1}^N a_i}. \quad (3.4)$$

Matched filter method uses the empirical template  $h_i$  for the pulse shape firstly, and then uses the template to match the echo pulse to get a correlation sequence. The correlation sequence is given by

$$cor_i = \sum_{j=1}^N a_j h_{i+j}. \quad (3.5)$$

$T_C$  is obtained from the time sample giving  $\max cor_i$ . Matched filter method reduces uncertainty to a large extent and therefore removes noise efficiently [38], while it is more complicated to implement than center of mass method.

### 3.1.3 Resolution

Ultrasound image quality highly depends on the resolution. Ultrasound imaging resolution can be divided into three categories: spatial resolution, temporal resolution and contrast resolution [39]. This section only describes the spatial resolution. Spatial resolution is the ability of an ultrasound system to distinguish two nearby points and is

determined mainly by the transducer. Spatial resolution includes lateral resolution and axial resolution. Lateral resolution is the smallest distance between two points aligned perpendicular to the direction of ultrasound beam that can be resolved. The figure below shows the lateral resolution.

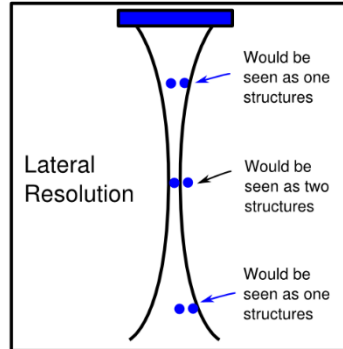


Figure 3.4: Lateral resolution [40]

Lateral resolution is determined by the beam diameter at the focal distance. Lateral resolution  $s_l$  therefore can be estimated by

$$s_l = BD \approx 1.028F_N\lambda. \quad (3.6)$$

Where  $BD$  is the beam diameter at the focal depth that is defined in previous section. High resolution system therefore uses high frequency with small  $F_N$ .

Axial resolution is the smallest distance between two points aligned to the direction of ultrasound beam that can be differentiated. The figure below shows the axial resolution.

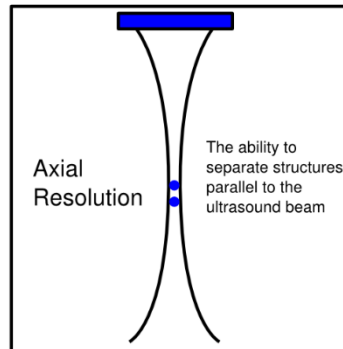


Figure 3.5: Axial resolution [42]

For pulse ultrasound systems the axial resolution is determined by the pulse length  $pl$  in the time domain and the sound velocity  $c$ . Axial resolution  $s_a$  can be estimated by

$$s_a \approx \frac{c * pl}{2}. \quad (3.7)$$

Based on the above formula, a small  $s_a$  therefore requires the transducer with high bandwidth which can generate short pulses.

### 3.1.4 Noise

There are many types of noise in ultrasound imaging. The presented noise depends on the specific application. Such as speckle noise and electronic noise are often considered in ultrasound imaging. Speckle noise is considered to be multiplicative, so its reduction is more complicated than for example reduction of electronic noise which is often viewed as additive noise [41].

When interactions occur in many sub-resolution scatters, complex interference patterns called speckle will be produced. Speckle is considered as granular or mottled texture with rapid spatial change, which is often mistaken for real structure [42]. Speckle is detrimental because it both blurs the object edges and reduce contrast in ultrasound images. It is therefore quite necessary to reduce speckle in ultrasound images. Many methods of speckle reduction have been proposed such as frequency compounding, spatial compounding and post filtering [43].

### 3.1.5 Imaging modes

There are many ultrasound imaging modes based on pulse echo technique. A mode, B mode, 3D mode and 4D mode are typically based on pulse echo technique. A mode is short for amplitude modulation mode which is the simplest mode in ultrasound imaging. A mode imaging means that a single transducer scans a line through the objects with the echoes plotted on the screen as a function of depth [44].

B mode is known as brightness mode or 2D mode which is most widely used for medical ultrasound imaging. B mode image shows the amplitude in the 2D plane scanned by transducer. An example of B mode image is shown below.



Figure 3.6: An example of B mode image showing human tissues [45]

3D mode refers specifically to volume rendering of ultrasound data. Usually multiple imaging planes are needed to construct the 3D image. The main challenge of 3D mode or imaging is that the positions and orientations of all planes need to be identified. The figure below shows the 3D reconstruction using several 2D images.

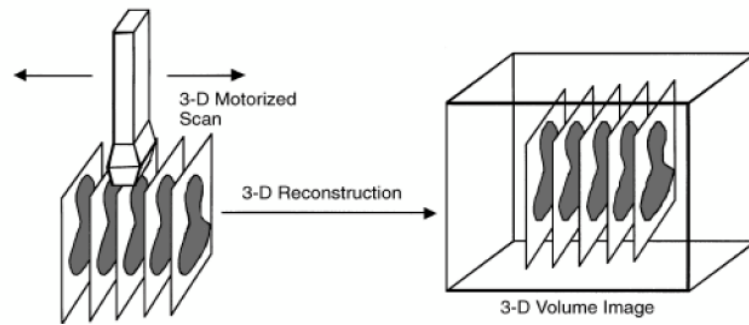


Figure 3.7: 3D ultrasound reconstruction [46]

4D mode is the time dependent 3D mode. To construct 4D image, time and position information is necessary for every acquired plane. 3D and 4D images are simpler to interpret than 2D images while the amount of data for 3D and 4D images is much larger than that of 2D images.

### 3.2 Matched filter

In addition to speckle noise, gaussian noise is a kind of additive noise which may originated from electronic equipment or experiment environment in ultrasound imaging. Matched filter is the optimal linear filter to obtain the highest signal to noise ratio (SNR) in the presence of the additive gaussian noise [47]. The rest part of this section describes the derivation of matched filter.

The signal processing steps of a linear filter is shown below.

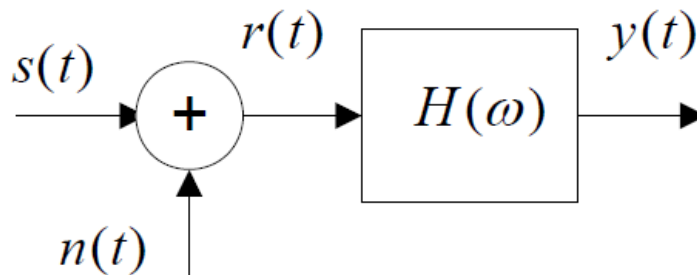


Figure 3.8: Signal processing flow of a linear filter

Where  $s(t)$  is the input signal,  $n(t)$  is the gaussian noise, and  $r(t)$  is the signal received by the filter.  $H(w)$  is the frequency response of the filter and  $y(t)$  is the output. Assume  $H(w)$  is the frequency response of the optimal linear filter.

$$r(t) = n(t) + s(t), \quad (3.7)$$

$$y(t) = n_0(t) + s_0(t). \quad (3.8)$$

Where  $n_0(t)$  is the output noise and  $s_0(t)$  is the desired output signal. The spectrum of  $s(t)$  is noted as  $S(w)$ , the spectrum of  $s_0(t)$  is  $S_0(w)$ , and the two-sided power

spectrum density of  $n(t)$  is noted as  $\frac{n_0}{2}$ .  $s_0(t)$  can be represented as

$$s_0(t) = \frac{1}{2\pi} \int_{-\infty}^{+\infty} S_0(w) e^{j\omega t} dw. \quad (3.9)$$

The average power of output noise  $N_0$  is defined as

$$N_0 = \frac{n_0}{4\pi} \int_{-\infty}^{+\infty} |H(w)|^2 dw. \quad (3.10)$$

At time  $t_0$ , the ratio of output instantaneous power to noise average power is

$$r_0 = \frac{|s_0(t)|^2}{N_0} = \frac{\left| \frac{1}{2\pi} \int_{-\infty}^{+\infty} S_0(w) e^{j\omega t} dw \right|^2}{\frac{n_0}{4\pi} \int_{-\infty}^{+\infty} |H(w)|^2 dw}. \quad (3.11)$$

According to Cauchy–Schwarz inequality, the above equation can be changed as

$$r_0 \leq \frac{\frac{1}{2\pi} \int_{-\infty}^{+\infty} |S(w)|^2 dw}{\frac{n_0}{2}}. \quad (3.12)$$

According to Plancherel theorem, the energy of input signal  $E$  can be defined as

$$E = \int_{-\infty}^{+\infty} |S(w)|^2 dw = \int_{-\infty}^{+\infty} |s(t)|^2 dt. \quad (3.13)$$

Combining Eq. (3.12) and (3.13) we have the following formula

$$r_0 \leq \frac{2E}{n_0}. \quad (3.14)$$

The maximum SNR therefore is  $\frac{2E}{n_0}$  in the presence of white gaussian noise. The impulse response of the linear filter at the time point when SNR reaches maximum is

$$h(t) = \begin{cases} s(T-t), & t \geq 0 \\ 0, & t < 0 \end{cases} \quad (3.15)$$

Where  $T$  is the length of the input signal.  $h(t)$  is the so-called Matched filter.

### 3.3 Coded excitations

#### 3.3.1 Basic Principles

In practical ultrasound imaging system,  $s(t)$  can be considered as the excitation to the

ultrasound transducer. We can therefore see that the maximum SNR for ultrasound imaging system is  $\frac{2E}{n_0}$ . The maximum SNR is independent of pulse bandwidth and methods of modulation, and only associated with the input signal energy and the noise power density [48]. Therefore, SNR can be improved by increasing the energy of the input signal. To increase the energy of the input signal, one way is to increase the amplitude of the input signal, and another way is to increase the time span of the input signal. For security reasons, the peak amplitude of the ultrasound pulse should be under a certain limitation. The reasonable way therefore is to increase the time span. However, if only simply increase the time span of the excitation signal, the axial resolution would become worse. Coded excitation technique can be used to solve this problem properly. Coded excitation technique uses long coded pulse to increase the energy without increasing the peak amplitude of the pulse. The block diagram of coded ultrasound system is shown below.

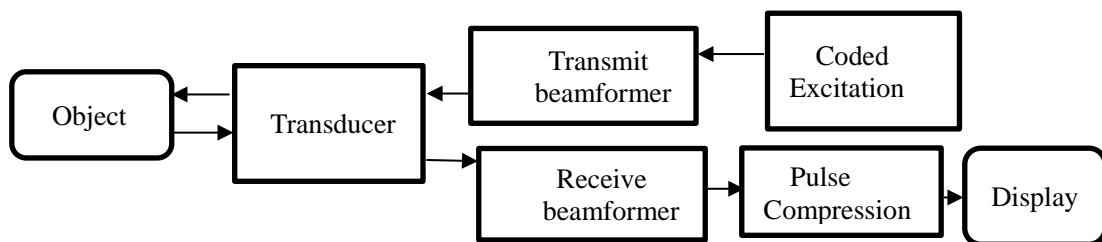


Figure 3.9: Block diagram of coded ultrasound system

Compared to the conventional pulse echo ultrasound imaging system, the coded excitation system has two major differences. The first difference is that coded excitation system uses long pulses instead of short pulses. The second difference is that for coded excitation system the received pulses need to be compressed to keep the axial resolution. The basic principle of coded excitation is shown in the following figure.

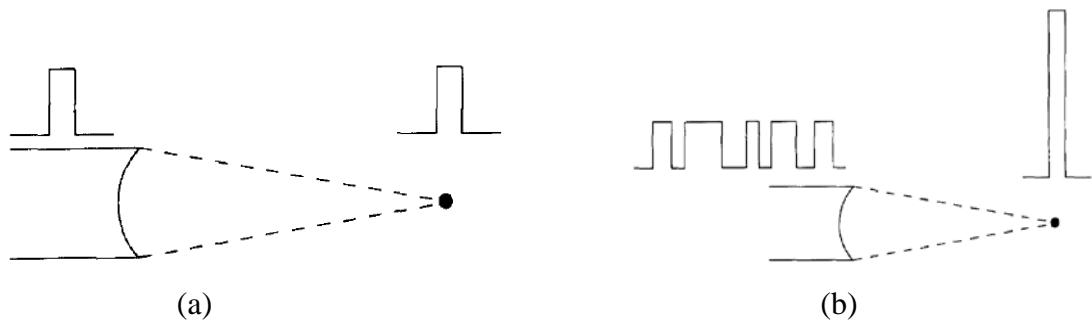


Figure 3.10: Basic principle of Coded excitation. (a) Conventional pulse excitation. (b) Coded excitation [49]

Let the signal received by the Matched filter have an average power  $S$  over the pulse duration  $T$ . The average noise power within the received signal bandwidth  $B$  is  $BN_0$ . For narrowband signals, the average power at any time instance is roughly half the instantaneous peak power at the same time instance. Then the gain in SNR (GSNR) after processed by the Matched filter is [50]

$$GSNR = \frac{SNR_{out}}{SNR_{in}} = \frac{\frac{2E}{N_0}/2}{S/BN_0} = TB. \quad (3.16)$$

The increment of SNR equals to the time-bandwidth product of the received signal. From the above formula, the increment of time or bandwidth of excitation can all lead to improvement of SNR. There might be a confusion that the input of the Matched filter is the pulse transmitted by the ultrasound transducer while the coded excitation is the input of the ultrasound transducer. In practical, the excitation to the ultrasound transducer is coded instead of the pulse transmitted by the transducer. In theory analysis, the excitation to transducer can be considered as the input to the Matched filter, and the ultrasound transducer is viewed as a bandpass filter. The influence of transducer on the coded excitation is considered separately [51].

### 3.3.2 Evaluation Criteria

SNR, axial resolution and contrast are important parameters to evaluate the quality of ultrasound images. The maximum SNR in theory is  $\frac{2E}{n_0}$ , while in practical the SNR cannot reach  $\frac{2E}{n_0}$  because of the attenuation, use of Mismatched filter and etc. Usually the transmitted waveforms cannot be compressed ideally similar to the waveform in Figure 3.10 (b). The clutter exists in the compressed wave in addition to the central high amplitude response. Even the complementary Golay codes from which the clutter can be cancelled theoretically cannot reach an ideal result like the waveform in Figure 3.10 (b) due to the attenuation or other reasons in practical application [16]. In coded excitation ultrasound imaging, mainlobe width and range sidelobe level are two important criteria to evaluate the effect of coded excitations [48].

Figure 3.11 illustrates a compressed wave. The central high amplitude response is the mainlobe. The mainlobe width  $\Delta\tau$  is the distance between the points where the amplitude is half of the peak amplitude [52]. The clutter around the mainlobe are the range sidelobes.

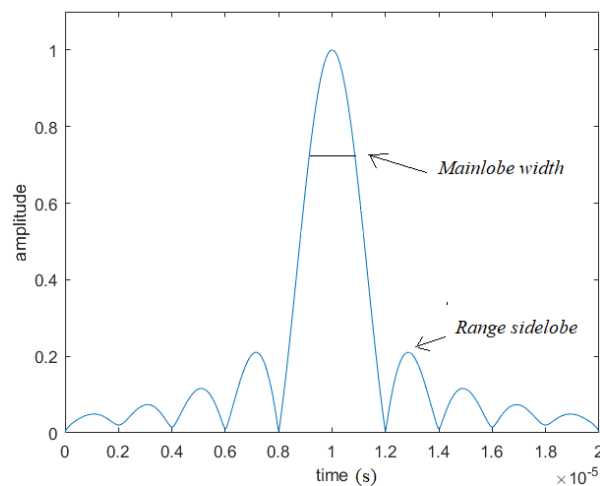


Figure 3.11: Mainlobe and sidelobes of a compressed wave

The axial resolution of the imaging system  $\Delta R$  is determined by mainlobe width  $\Delta\tau$  that is defined as

$$\Delta R = c \cdot \Delta\tau. \quad (3.17)$$

The narrower the mainlobe width, the better the axial resolution. -20 dB and -6 dB mainlobe width are also often used to measure the axial resolution [16] [51] [53].

Coded excitations have many benefits such as improvement of SNR and increment of penetration distance while sidelobes are inevitable as long as the coded excitations are implemented. Range sidelobe level is often evaluated by peak sidelobe level PSL and integrated sidelobe level ISL. They are given by

$$PSL = 20 \lg \frac{\max(A_{side})}{\max(A_{main})}, \quad (3.18)$$

$$ISL = 10 \lg \frac{\text{sidelobe power}}{\text{mainlobe power}}. \quad (3.19)$$

Where  $\max(A_{side})$  and  $\max(A_{main})$  are the peak amplitude of the mainlobe and sidelobe respectively. Therefore, small PSL and ISL are needed to obtain an image with high contrast.

### 3.3.3 Chirp excitation

The selection of coded excitations has a great impact on the imaging quality in code excitation ultrasound systems. A proper coded excitation should make the mainlobe width narrow and the range sidelobe small. Frequently used coded methods are frequency modulation and phase modulation [51]. Chirp signal is one of the most widely used frequency modulated signal. The theory of chirp coding in this section is referred from two books *Radar Signals: An Introduction to Theory and Application* and *High-Resolution Radar* [50] [54].

Chirp signal is also called linear frequency modulated signal that can be defined as

$$s(t) = a(t)e^{j2\pi(f_0 t + \frac{B}{2T}t^2)}, \quad -\frac{T}{2} \leq t \leq \frac{T}{2}. \quad (3.20)$$

Where  $f_0$  is the center frequency of the chirp signal,  $T$  is the duration, and  $B$  is the bandwidth.  $s(t)$  can also be written into the real form with a positive time dependent, but complex form is easy for arithmetic operation. The instantaneous frequency is

$$f_i = \frac{d(f_0 t + \frac{B}{2T}t^2)}{dt} = f_0 + \frac{B}{T}t. \quad (3.21)$$

Where  $B/T$  is the frequency rate that controls the velocity of frequency change. The frequency range swept by the chirp signal is  $[f_0 - B/2, f_0 + B/2]$ . Therefore, the time-

frequency product namely the SNR gain is  $TB$ . SNR gain is associated with the time duration and bandwidth. SNR gain can be improved by increasing the duration or bandwidth. While the bandwidth is limited by the ultrasound transducer which is considered as a bandpass filter, increasing the duration is often the method to improve SNR gain. Assume  $a(t)$  is the rectangular signal  $rect(t/T)$ , the complex envelope of the Chirp signal is

$$env(t) = rect(t/T)e^{j\pi(\frac{B}{T})t^2}. \quad (3.22)$$

Considering that there is no attenuation, the output signal of matched filter is given by

$$R(t_1) = \int_{-\infty}^{+\infty} s(t) s^*(t + t_1) dt. \quad (3.23)$$

Where  $s^*(t + t_1)$  means the complex conjugate of  $s(t + t_1)$ . Combining (3.22) and (3.23),  $R(t_1)$  is rewritten as

$$R(t_1) = Te^{-j2\pi f_0 t_1} \frac{\sin \left[ \pi B t_1 \left( 1 - \frac{|t_1|}{T} \right) \right]}{\pi B t_1}. \quad (3.24)$$

As is shown in the above equation, the output signal is similar to *sinc* function which has many sidelobes. Sidelobes are the major drawback of coded excitation. To eliminate sidelobes, windowing operations are often added to the Chirp signal or Matched filter. The figure below shows the compressed signals without and with Blackman window.

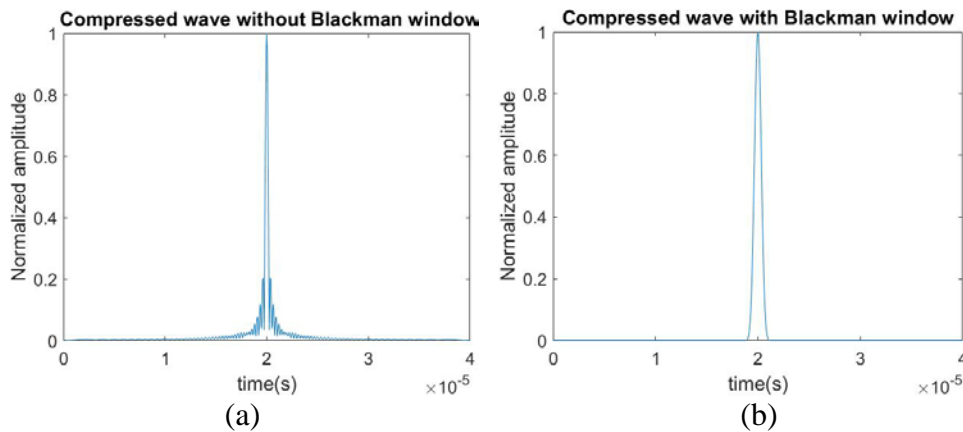


Figure 3.12: Compressed wave. (a) Without Blackman window. (b) With Blackman window

It can be concluded from the above figure that sidelobes of the compressed wave after windowing operation are eliminated greatly, while the mainlobe width is widen to some extent. Windows such as Blackman window is good for reducing the sidelobes near the mainlobe while the distant sidelobes are not controlled by windows. This is due to the Fresnel ripples. Usually phase and amplitude predistortion are used to eliminate the distant sidelobes [51].

Compared with conventional excitation, Chirp signal has high time-bandwidth product

which leads to better SNR gain. Conventional ultrasound imaging usually uses a short pulse to excite the transducer. Simply using long pulse is not a proper method to gain high SNR since the time-bandwidth does not change much. This is because usually large time width in time domain means a narrow width in frequency domain. The figure below show three signals and their spectrum. Figure 3.13(a) and 3.13(b) are the conventional short pulse and its spectrum. Although the frequency bandwidth is wide in 3.13(b), the time-bandwidth is small because of the short time duration. Figure 3.13(c) and 3.13(d) are the long pulse and its spectrum. Although the time duration is large in 3.13(c), the time-bandwidth is small because of the narrow frequency spectrum. Figure 3.13(e) and 3.13(f) are Chirp signal and its spectrum. The time-frequency product of Chirp signal is the largest among three signals because of its long time duration and wide frequency spectrum.

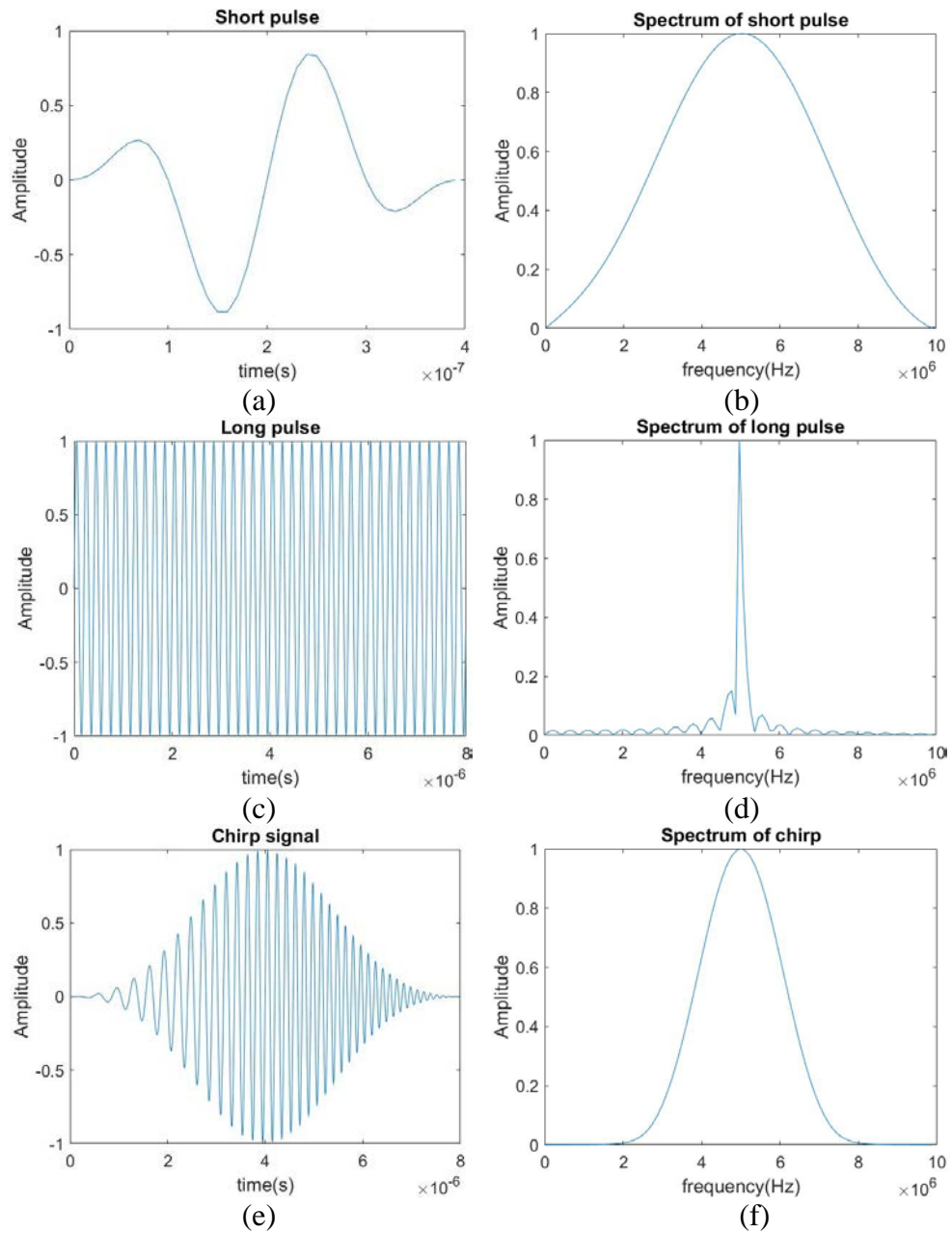


Figure 3.13: Signals and their spectrum. (a) Short pulse. (b) Spectrum of short pulse. (c) Long pulse. (d) Spectrum of long pulse. (e) Chirp signal. (f) Spectrum of Chirp signal

### 3.3.4 Phase modulation and Barker excitation

The fundamental principle of phase modulation is a recomposition of phases in a signal in order to cancel out the correlation integral away from the origin [51]. Barker excitation is a commonly used phase modulated excitation. The theory of phase modulation and barker excitation in this section is referred from the book *Radar Signals: An Introduction to Theory and Application* and Misaridis' thesis *Ultrasound Imaging Using Coded Signals* [50] [51].

A typical phase modulated signal can be given by

$$s(t) = a(t)e^{j2\pi f_0 t} e^{j\varphi(t)}. \quad (3.25)$$

For binary phase modulation, the phase modulation function  $\varphi(t)$  can only be 0 and  $\pi$ . For convenience,  $e^{j\varphi(t)}$  is usually represented by the sequence  $C_k = e^{j\varphi(t)} = \pm 1$ . Assume  $a(t)$  is given by

$$a(t) = \begin{cases} \frac{1}{\sqrt{NT_0}}, & 0 < t < NT_0, \\ 0, & \text{else} \end{cases} \quad (3.26)$$

where  $N$  is the length of sequence and  $T_0$  is the time duration of single sub-pulse. The complex envelope of the binary phase modulated signal is

$$env(t) = \begin{cases} \frac{1}{\sqrt{N}} \sum_{k=0}^{N-1} C_k \vartheta(t - kT_0), & 0 < t < NT_0, \\ 0, & \text{else} \end{cases} \quad (3.27)$$

$env(t)$  can also be represented by

$$env(t) = env_1(t) * env_2(t). \quad (3.28)$$

Where  $*$  is convolution operation.  $env_1(t)$  and  $env_2(t)$  are given by

$$env_1(t) = \begin{cases} \frac{1}{\sqrt{T_0}}, & 0 < t < T_0, \\ 0, & \text{else} \end{cases} \quad (3.29)$$

$$env_2(t) = \frac{1}{\sqrt{N}} \sum_{k=0}^{N-1} C_k \delta(t - kT_0). \quad (3.30)$$

Based on the convolution theorem of Fourier transform, the spectrum of the complex envelope  $env(t)$  is

$$ENV(f) = ENV_1(f)ENV_2(f). \quad (3.31)$$

Where  $ENV_1(f)$  and  $ENV_2(f)$  are

$$ENV_1(f) = \sqrt{T_0} \text{sinc}(fT_0) e^{-j\pi f T_0}, \quad (3.32)$$

$$ENV_2(f) = \frac{1}{\sqrt{N}} \sum_{k=0}^{N-1} C_k e^{-j\pi f k T_0}. \quad (3.33)$$

The power spectrum of  $env(t)$  is

$$|ENV(f)|^2 = |ENV_1(f)|^2 |ENV_2(f)|^2. \quad (3.34)$$

$|ENV(f)|^2$  can be represented by

$$|ENV(f)|^2 = \frac{1}{N} \left[ N + 2 \sum_{m=1}^{N-1} X_b(m) \cos(2\pi f m T_0) \right] |ENV_1(f)|^2. \quad (3.35)$$

Where  $X_b(m)$  is defined by

$$X_b(m) = \sum_{k=0}^{N-1-m} C_k C_{k+m} = \begin{cases} N, & m = 0 \\ a \ll N, & m \neq 0 \end{cases} \quad (3.36)$$

Therefore  $|ENV(f)|^2 \approx |ENV_1(f)|^2$ . The spectrum width of binary phase modulated signal is close to that of sub-pulse. Then the time-bandwidth product of binary phase modulated signal becomes  $NT_0B$  which is much larger than that of the simple single pulse  $T_0B$ . An example of a binary phase modulated signal, barker coded signal, is shown in Figure 3.14.

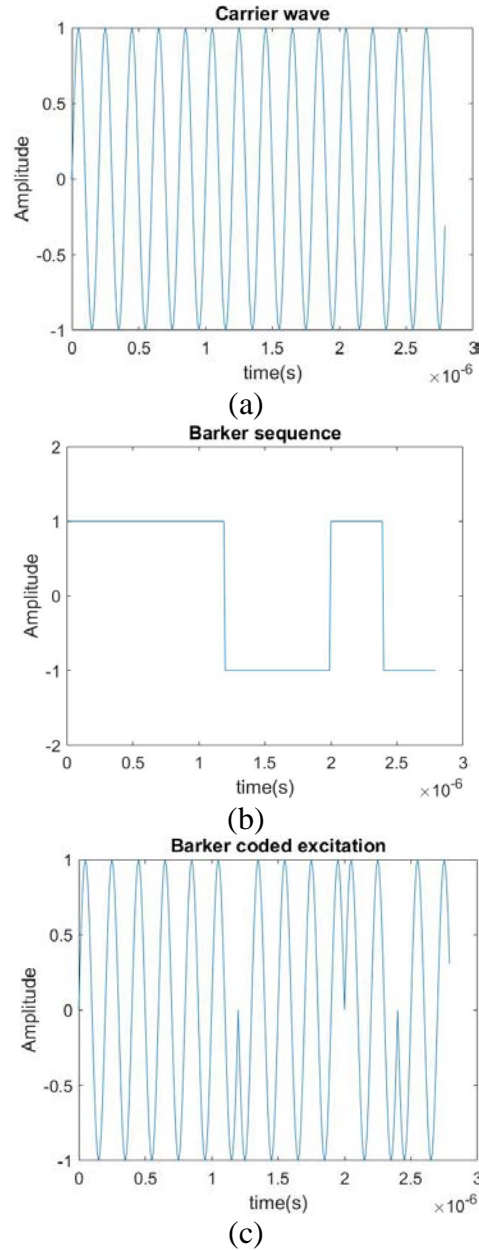


Figure 3.14: Barker code ( $N = 7$ ). (a) Carrier wave. (b) Barker sequence. (c) Barker coded excitation

Barker code is considered to be an ideal code for coded excitation because of its low sidelobes in auto-correlation function. The sidelobes can only have three values 0, 1 and -1. For a barker sequence  $\{b_1, b_2, b_3, \dots, b_N\}$  with length  $N$ , its auto-correlation is given by

$$C(j) = \sum_{i=1}^{N-1} b_i b_{i+j} = \begin{cases} N & j = 0 \\ 0 \text{ or } \pm 1 & 0 \leq j \leq N. \\ 0 & j \geq N \end{cases} \quad (3.37)$$

From equation (3.37) we can see that the ratio of amplitude of mainlobe to sidelobe in barker sequence is  $N$ , which shows the good compression quality. And that the amplitude of sidelobes is same. When the length of barker sequence is 13, the peak sidelobe level

reaches minimum -22.2 dB. Figure 3.15 shows auto-correlation of barker code with  $N = 7$ . Table 3.1 lists the seven proposed barker sequences.

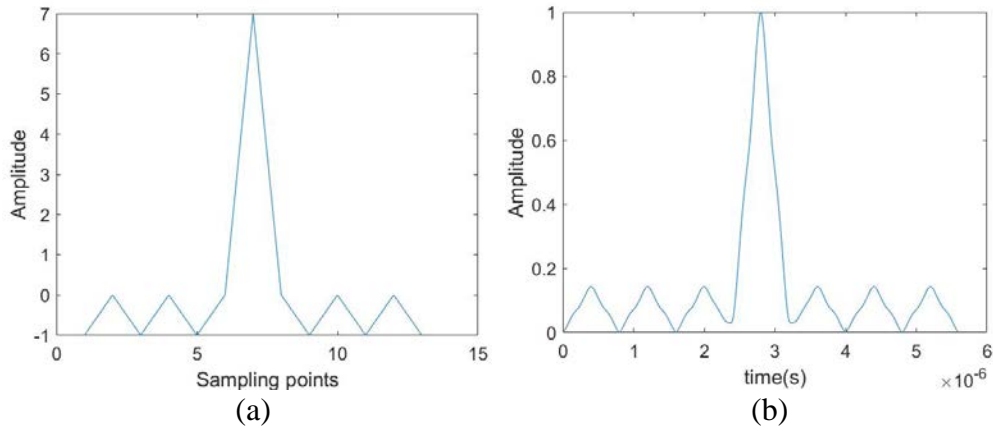


Figure 3.15: Auto-correlation. (a) Auto-correlation of barker sequence. (b) Auto-correlation of barker coded excitation

$N$	Barker sequence	Peak sidelobe level (dB)
2	1, 1 or 1, -1	-6
3	1, 1, -1	-9.6
4	1, 1, 1, -1 or 1, 1, -1, 1	-12
5	1, 1, 1, -1, 1	-14
7	1, 1, 1, -1, -1, 1, -1	-17
11	1, 1, 1, -1, -1, -1, 1, -1, -1, 1, -1	-20.8
13	1, 1, 1, 1, 1, 1, -1, -1, 1, 1, -1, 1, -1, 1	-22.2

Table 3.1: Barker sequences

### 3.4 Mismatched filter

In coded ultrasound imaging system, the echo pulses received by the transducer are also long pulses same with the long coded excitation. These long echo pulses are usually compressed into short pulses using filters, and the compression process is called wave compression. The object of wave compression is to gain high SNR and keep axial resolution in the meantime. The simplest filter to reach the object is Matched filter. However, the range sidelobe level is not small enough in some situations. Therefore, Mismatched filters are often used to eliminate the sidelobes. One way of generating Mismatched filter is windowing the Matched filter, and this kind of Mismatched filter is also called weighted matched filter. For Mismatched filter, the reducing of range sidelobe level is at the price of increasing the mainlobe width, so there is always a trade-off between mainlobe width and range sidelobe level [55]. In addition to weighted matched filter, Mismatched filters such as inverse filter and Wiener filter are also widely used in pulse compression.

To obtain a compressed wave that approaches the delta function, the product of spectrum of input signal and filter should be a constant. A filter meet this requirement is the so-called inverse filter. The transfer function of inverse filter is given by [56]

$$H(f) = \frac{1}{C(f)} = \frac{C^*(f)}{C(f)C^*(f)} = \frac{C^*(f)}{|C(f)|^2}. \quad (3.38)$$

Where  $H(f)$  is the transfer function of inverse filter, and  $C(f)$  is the spectrum of the input signal. If  $C(f)$  have zero crossings,  $H(f)$  does not exist. And if  $C(f)$  changes abruptly,  $H(f)$  could be very sensitive to noise so that SNR would be severely affected. To avoid zero-crossing problem, Wiener filter can be used. Transfer function of Wiener filter is defined as

$$H(f) = \frac{C^*(f)}{C(f)C^*(f) + N_f(f)N_f^*(f)}. \quad (3.39)$$

Where  $N_f(f)$  is the spectrum of the noise. For coded ultrasound imaging system, the optimum filter is Wiener filter in the presence of white gaussian noise and speckle noise [51]. If the filter is designed for reducing the speckle noise and white gaussian noise, the transfer function of Wiener filter is adjusted as

$$H(f) = \frac{C^*(f)}{k_c|C(f)|^2 + \lambda}. \quad (3.40)$$

Where  $\lambda$  is the power spectrum of the noise,  $k_c$  is the mean scattering strength. If  $\lambda$  is quite large, Wiener filter degenerates to Matched filter. If  $\lambda$  is quite small, Wiener filter degenerates to inverse filter. The problem of building a filter defined by Eq. (3.40) is that  $k_c$  relatively to the noise level is usually unknown [51].

## Chapter 4

### Experiment implementation

This chapter gives a description of the experiment used in this thesis. It concludes the illustration of physical setup and data processing part of the experiment. The experimental work is the key part of the thesis. Various coded pulses are designed as the input of the transducers. Two different transducers are used to generate pulses.

The goals of the experiment are discussed firstly, and then the flow of the experiment is described. The equipment and cartilage sample are presented in the following section. The last part of this chapter mainly illustrates the data processing techniques needed in the experiment.

#### 4.1 Goals of experiment

The main purpose of the experiment is to evaluate the uses of coded excitations in ultrasound imaging. Under some specific imaging conditions, reception of reliable ultrasound signals is challenging due to a very low signal to noise ratio (SNR) which leads to poor quality images. First, we wanted to study the performance of the coded excitations, by isolating factors such as decoding methods. Then we looked into the performance of the decoding methods. The quality of two different transducers are also investigated during the process.

#### 4.2 Experiment flow

The experiment consists of two major parts. First part is scanning and data recording, the second part is data processing. Both scanning and data recording were performed by designated software written in LABVIEW. Data processing is performed by MATLAB.

For the scanning and data recording part, a customized ultrasonic scanning platform is built around Leica DMI8 inverted microscope, which is integrated with ASI MS-2000 XYZ high precision scanning stage. LabVIEW is used to control the scanning phase and other components of the microscope. The ultrasonic functionality was realized by using a PXI FPGA module and FlexRIO hardware from National Instruments. The FlexRIO hardware contains a waveform generator and an amplifier for pulse generation, and a high-speed digitizer for pulse recording. The scanning was carried out at room temperature and the focal point of the transducer was placed roughly in the depth of half thickness of the sample. An overview of the scanning and data recording system is shown in Figure 4.1. Figure 4.1 is only an overview of the scanning system, some components such as attenuator and digitizer are not included. Data processing part of the experiment mainly includes time calibration, interpolation and filtering. A schematic diagram of the experiment flow is shown in Figure 4.2.

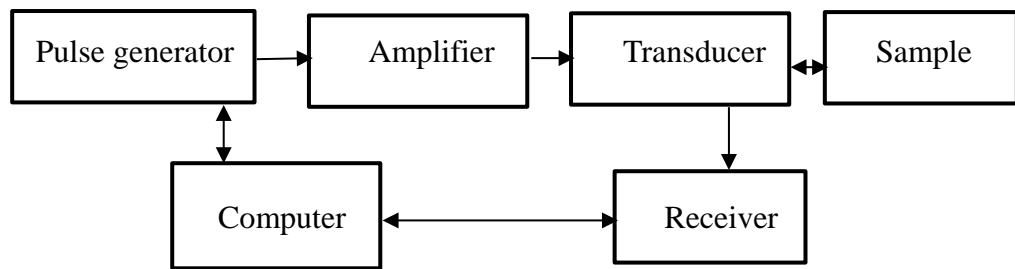


Figure 4.1: Schematic overview of the ultrasonic scanning system

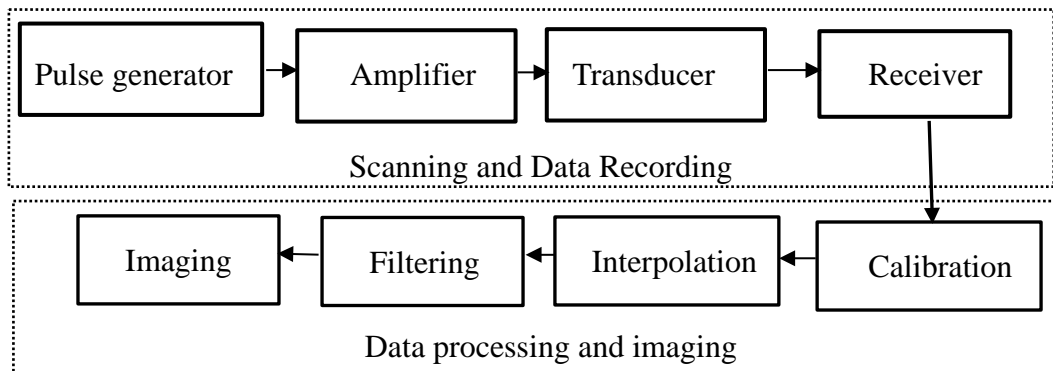


Figure 4.2: Schematic diagram of the experiment flow

In terms of the specific content of the experiment, the experiment can be categorized into 8 cases. The classification of cases is based on the excitations, transducers and whether the received signal is averaged in the experiment. All the cases are listed in the table under.

Case No.	Transducer	Excitation	average times
1	PZT	Ricker pulse	16 times
2	PZT	Ricker pulse	no average
3	PZT	Chirp	16 times
4	PZT	Barker	16 times
5	PVDF	Ricker pulse	16 times
6	PVDF	Ricker pulse	no average
7	PVDF	Chirp	16 times
8	PVDF	Barker	16 times

Table 4.1: Different cases used in the experiment

### 4.3 Equipment and cartilage sample

The main equipment used in the current study includes a scanning acoustic microscope

(SAM) (with signal generator, signal amplifier, signal receiver, scanning stage and transducers), and a petri dish used to immerse the sample in water. Two transducers mounted on the SAM are focused PVDF transducer and focused PZT transducer. Both the PVDF transducer and the PZT transducer made by OLYMPUS, have their center frequencies around 40 MHz. The imaging dish is a  $\mu$  – Dish 50 mm low IBIDI product. The detailed information of the transducers is in Appendix A and B. The cartilage sample is collected from a patient who underwent knee operation at the University Hospital of Northern Norway. A written informed consent is provided by the patient. The collected sample was cut into 1.0 to 1.5 mm slices and then stored in phosphate-buffered saline (PBS) solution for further ultrasonic scanning. The cartilage was attached on a substrate with medical tape when doing scanning, as is shown in Figure 4.3. We had cleared the liquid in the dish when the photo was taken. Actually, the cartilage was totally immersed into PBS solution when we did the experiment. Figure 4.4 shows the Leica inverted microscope used as the base for the SAM system. Figure 4.5 demonstrates the schematic representation of the PZT transducer we used, with a delay line denoted as the lens rod. The PVDF transducer on the other hand, is not using any internal delay line.

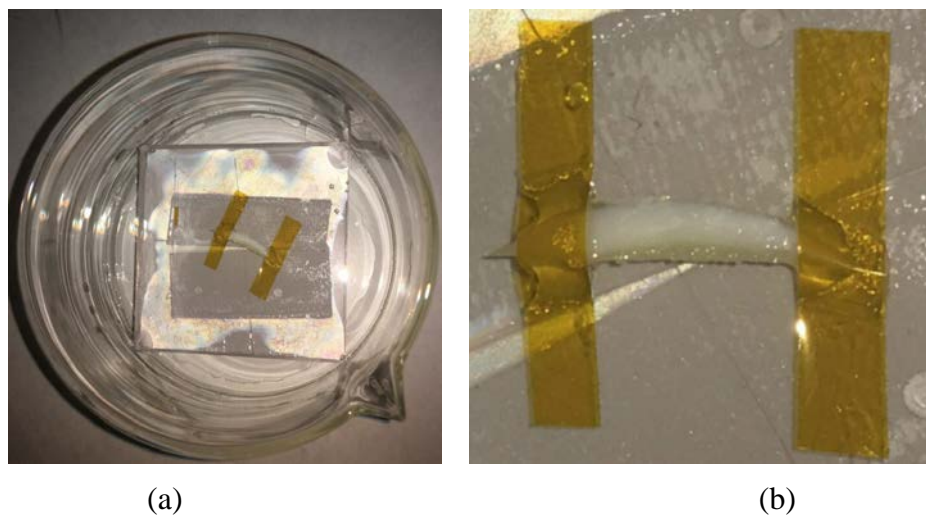


Figure 4.3: Human cartilage sample. (a) Original photo. (b) Zoomed in image

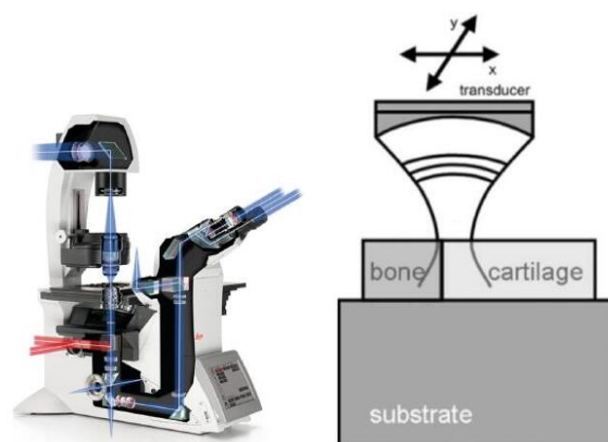


Figure 4.4: Scanning acoustic microscope [57]

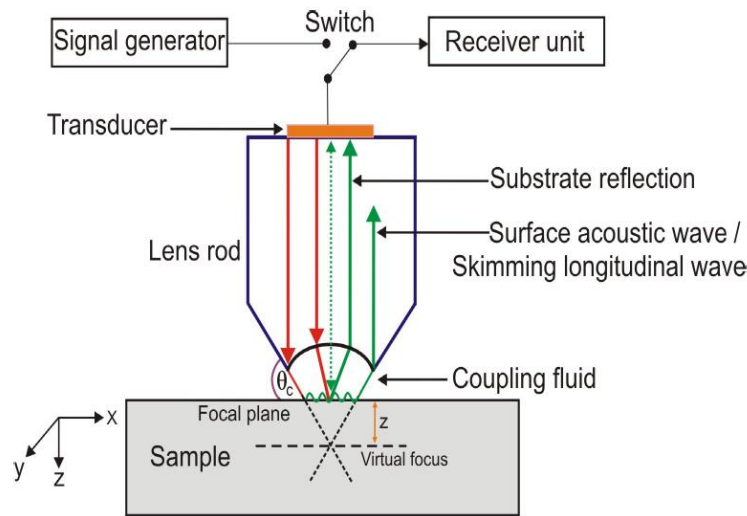


Figure 4.5: Schematic diagram of the PZT focused transducer [1]

## 4.4 Data processing

### 4.4.1 Time calibration

After recording all the data from scanning, data processing is needed both for calibration, wave compression, and for converting the data from time series into images. The first step of data processing is time calibration. The experimental scanning platform holding the samples has a slight misalignment compared to the transducer's normal plane (also known as the C-plane). This misalignment means that two reflections from a flat target separated by some distance, will gain a slight difference in time of flight. Therefore, we would like to compensate for unwanted time delay using a calibration method.

Since the scanning area is rectangular with some area without cartilage sample, we can use signals collected from this empty area as a reference to calibrate the signal's time axis. The scanning area is shown e.g. in Figure 4.6. Here we notice that the whole scanning area is a 5 mm x 3 mm rectangular where some of the area is without cartilage sample (shown as the brightest areas). More specifically, the scanning area is divided into 250 \* 150 pixels where every pixel corresponds a time series. An example of a time series for a chosen pixel is shown in Figure 4.7.

Time calibration mainly includes 4 steps. The first step is to compute the pulse locations for received pulses collected from 4 corners of the scanning area. Here maximum method and center of mass method are used instead of using the Matched filter method which requires much more computation time. The second step is to build a strictly flat time delay plane for the whole scanning area. Here we assume that the substrate, experiment platform and dish are absolutely flat. In a practical situation they are not absolutely flat, so our method will therefore not be perfect. The performance of this method is discussed in later chapter. The third step is to build up a time compensation plane while the fourth step is to do time shift for all the signals according to the time compensation plane.

Figure 4.8 shows signals collected from two positions of an empty area, it is obvious that

the two signals are not aligned. Theoretically, they should be aligned in time. This shows the importance of doing time calibration.

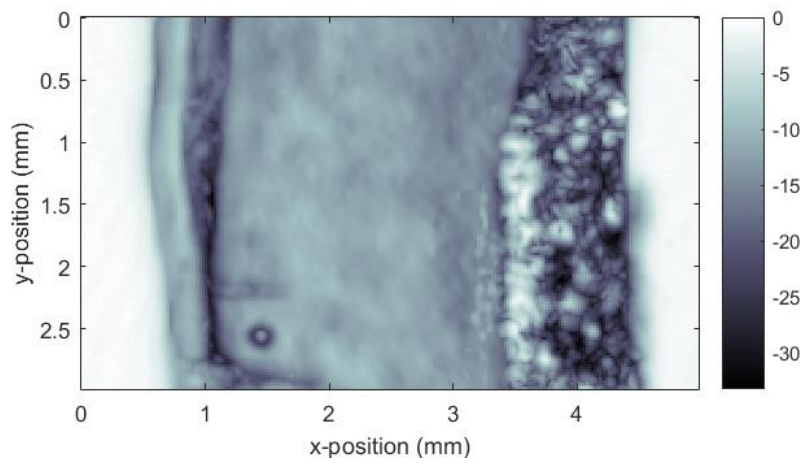


Figure 4.6: Cartilage sample

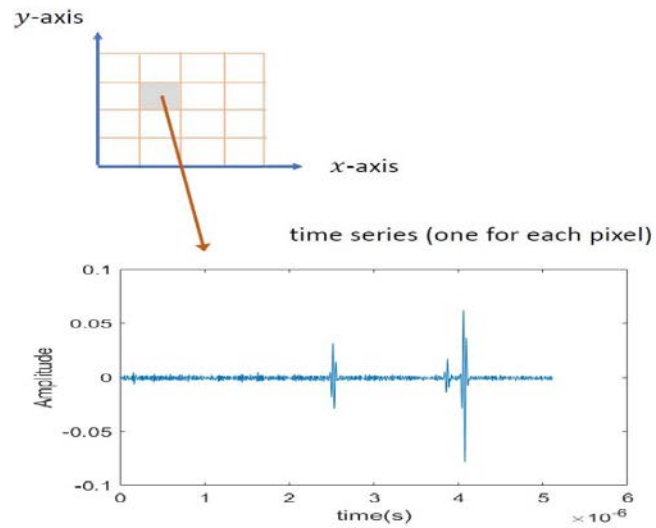


Figure 4.7: Time series of a pixel [57]

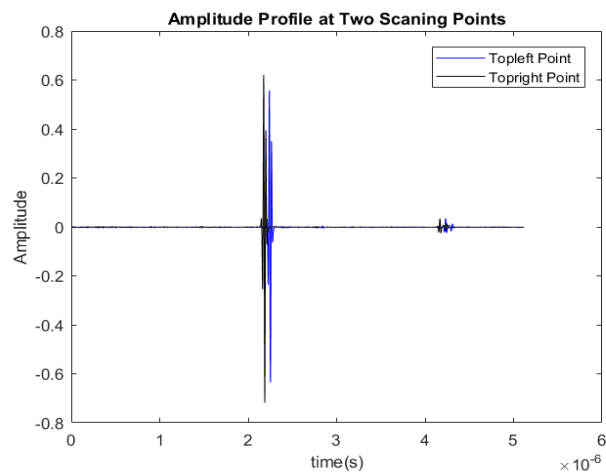


Figure 4.8: Two signals collected from two positions

### 4.4.2 Interpolation

The second step of the data processing will be interpolation. This is because the sampling frequency of the excitation signal and the sampling frequency of the received signal are different. The sampling frequency of the signal generator (through its DA converter) generating the excitation wave is 1.25 GHz while the signals received by the analogue electronics is sampled with 400 MHz in the experiment. The received signal is therefore interpolated to have the same sampling rate with the excitation signal.

Commonly used interpolation methods like piecewise constant interpolation, linear interpolation, polynomial interpolation and spline interpolation [58] were considered. From these methods we found the Spline interpolation method to be preferred for our experimental data.

### 4.4.3 Filtering

The third step which also will be a vital step in the data processing, is filtering. Two filters known as the Matched filter and Wiener filter were investigated in the filtering process. Both of the filters can be implemented in either the frequency domain or in the time domain. For each type of filter, both excitation signals and reflection signals can be used as template to generate the filters. For case 3, there therefore are 4 kinds of filtering situations based on the specific filter applied in filtering. Case 4, 7 and 8 also have 4 filtering situations respectively. All the situations that we have considered are listed in Table 4.2.

<i>Case No.</i>	Excitation	Filter	Template
1	Ricker pulse	No	No
2	Ricker pulse	No	No
3	Chirp signal	Matched filter	Excitation
3	Chirp signal	Matched filter	Reflection
3	Chirp signal	Wiener filter	Excitation
3	Chirp signal	Wiener filter	Reflection
4	Barker signal	Matched filter	Excitation
4	Barker signal	Matched filter	Reflection
4	Barker signal	Wiener filter	Excitation
4	Barker signal	Wiener filter	Reflection
5	Ricker pulse	No	No
6	Ricker pulse	No	No
7	Chirp signal	Matched filter	Excitation
7	Chirp signal	Matched filter	Reflection
7	Chirp signal	Wiener filter	Excitation
7	Chirp signal	Wiener filter	Reflection
8	Barker signal	Matched filter	Excitation
8	Barker signal	Matched filter	Reflection
8	Barker signal	Wiener filter	Excitation
8	Barker signal	Wiener filter	Reflection

Table 4.2: Filtering situations

#### 4.4.4 Image generation

The last step of the data processing is imaging. It is desired to generate both B scan and C scan images from the experimental data. Here B scan means a scan taken in a plane vertical to the transducer surface. C scan means a scan taken in a plane parallel to the transducer surface. An illustration of B scan, C scan and D scan is shown in figure 4.9.

In the experiment, only a single C scan image at a specified depth is generated. The recorded data is a set of time series and time series can be converted to distance namely depth. However, the signal value of a certain depth cannot be used to map the cartilage at that depth since the presence of the noise. We therefore use the maximum amplitude of each pixel to map the C scan.

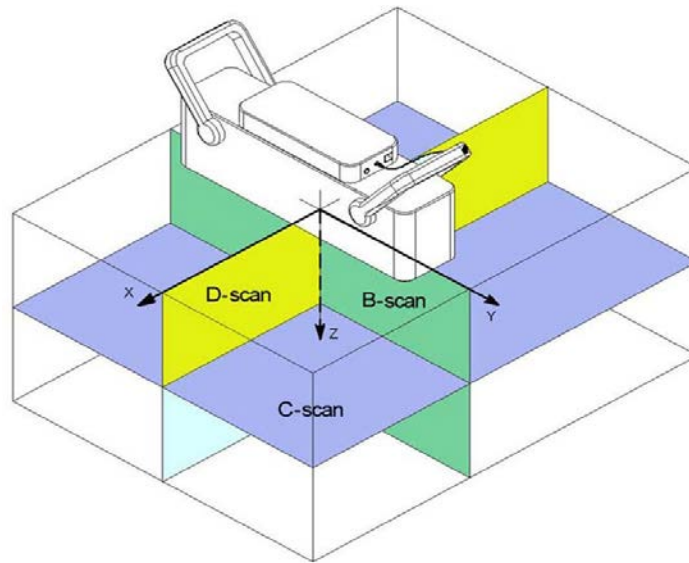


Figure 4.9: Schematic diagram of B scan, C scan and D scan [59]

## Chapter 5

### Results and discussion

In this chapter, the most essential experimental results are presented and discussed in details. The complete results obtained in this study can be downloaded from Munin UIT. Section 5.1 explains some practical details regarding implementing the excitation signals on the SAM platform. Section 5.2 discusses calibration needed to compensate for tilting of the scanning stage. Issues related to decoding methods are described in section 5.3. Discussion on PZT and PVDF transducers are presented in section 5.4. The last part of this chapter discusses the results in view of B scan of C scan images.

#### 5.1 Discussion on excitation signals

All the excitation signals used in the experiment are adjusted slightly from the theoretical formulas. The reasons for this adjustment are due to both the finite response time and frequency response of the transducer, and the fixed sampling times used by the signal generator (1.25 GHz) and digitiser (800 MHz) in the SAM system.

To minimize excitation of higher harmonics, unnecessary abrupt changes of excitation signal should be avoided, and the signals are therefore modified to become smoother. The coded waveform should also be adapted to the transducer's frequency response, e.g. with a typical bandpass response lacking DC values. One example of this is shown in Figure 5.1 yielding the Barker coded signal used in the experiment. The Barker coded signal is here implemented as a series of 13 Ricker waves since the shape of the Ricker wavelet match quite well with the transducer response. The Ricker waves are not simply connected one by one. At the junction between two Ricker waves, a short "zero" level is added to smooth the transition and give the transducer sufficient time to dynamically recover from the previous pulse.

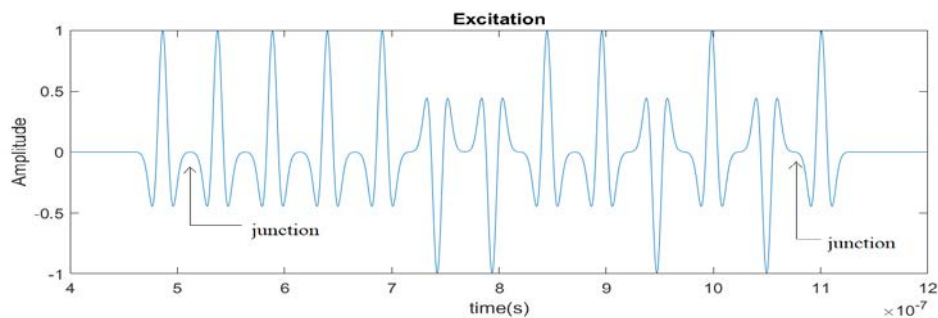


Figure 5.1: 13-bit Barker coded signal used in experiment

For the Chirp signal used in the experiment, the excitation pulse is defined by Eq. (5.1) instead of the simplest Chirp wave defined by Eq. (3.24). This is because the specific equation is found more convenient for controlling detailed waveform, and therefore more suitable and practical implementation in the ultrasonic scanning system. Eq. (5.1) is given as

$$Ch(\tau) = A \exp \left[ -\frac{(2\pi f)^2}{Q^2} (\tau - t)^2 \right] \exp \left\{ 2\pi i \left[ f(\tau - t) + \frac{d}{2} (\tau - t)^2 \right] \right\}, \quad (5.1)$$

where  $A = \left( \frac{8\pi f^2}{Q^2} \right)^{\frac{1}{4}}$ . In the formula  $t$  and  $f$  represent the center time and frequency respectively while  $Q$  is the dimensionless quality factor and set to be 80. The Chirp and Ricker waveforms used in the experiment are shown in Figure 5.2 (a) and (b), respectively.

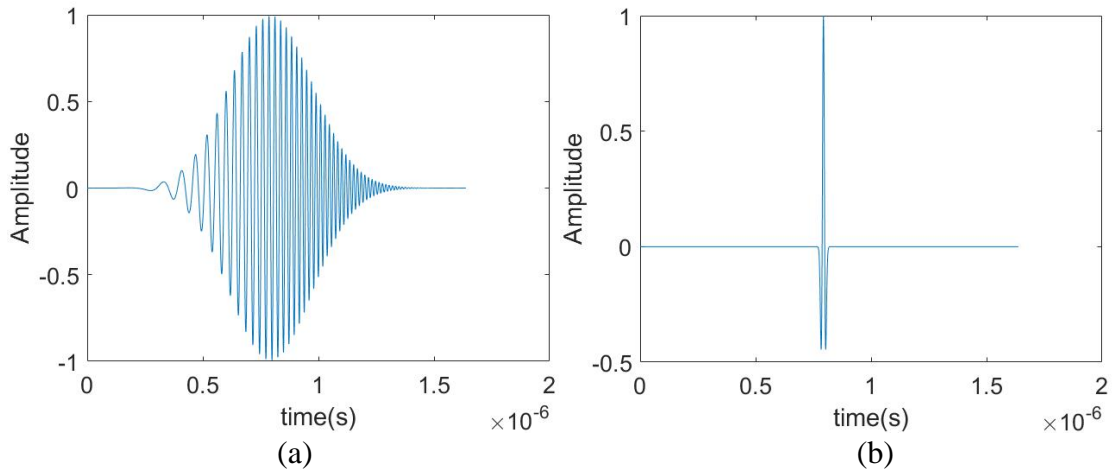


Figure 5.2: Excitations. (a) Chirp signal. (b) Ricker pulse.

To excite the ultrasonic transducer effectively, the spectrum of excitation signal has to be centred around the centre frequency of the ultrasonic transducer. The spectrums of the three used excitation signals are shown below. All the spectrums are centred around 40 MHz which is the centre frequency of the transducers used in the experiment. The bandpass shapes of these responses also match quite well with the measured transducer responses (provided by Olympus) shown in Appendix A and Appendix B.

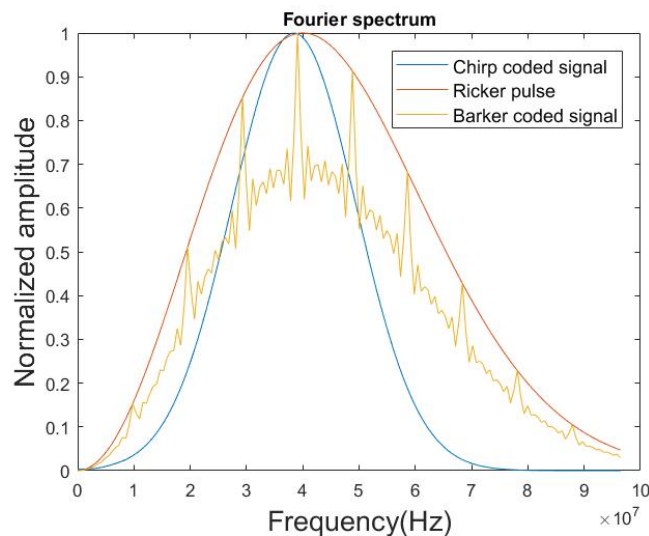


Figure 5.3: Spectrum

## 5.2 Discussion on time calibration

The received signals typically need to be calibrated and interpolated due to a small tilting of the scanning stage. A maximum amplitude method and centre of mass method are used to estimate the pulse location in the calibration operation, while a cubic spline method is used for interpolation between the time samples. To present some of the calibration results, we will mainly consider 2 different cases denoted as case 1 and 4.

Case 1 is used as an example to show the performance of calibration and interpolation. The signal before and after interpolation is shown in Figure 5.4. We can see that the cubic spline method works quite well for interpolation. Cubic spline method works well for all cases. The signals before and after time calibration are shown in Figure 5.5 (a) and (b). For time calibration, the used method of finding the pulse location is maximum method. The time delay and time compensation planes for the whole scanning area are shown in Figure 5.5 (c) and (d). Two signals are collected from top left (first scanning point) and top right scanning points. Since there is no cartilage at the two scanning points, the arriving time of the signals should be same if the two scanning points are at the same altitude. Before calibration the arriving time of the two signals is obviously different because of the tiled platform or similar reasons. After calibration, the signals are overlapped which shows that the performance of time calibration is good enough. Note that the signals in Figure 5.4 and Figure 5.5 are zoomed in to show the details.

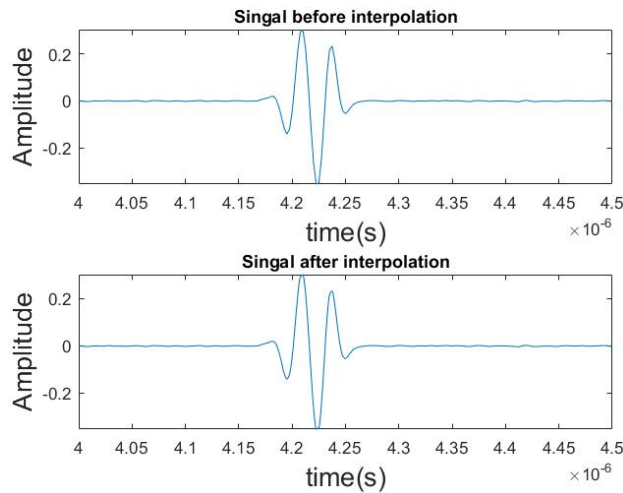


Figure 5.4: Signals before and after interpolation

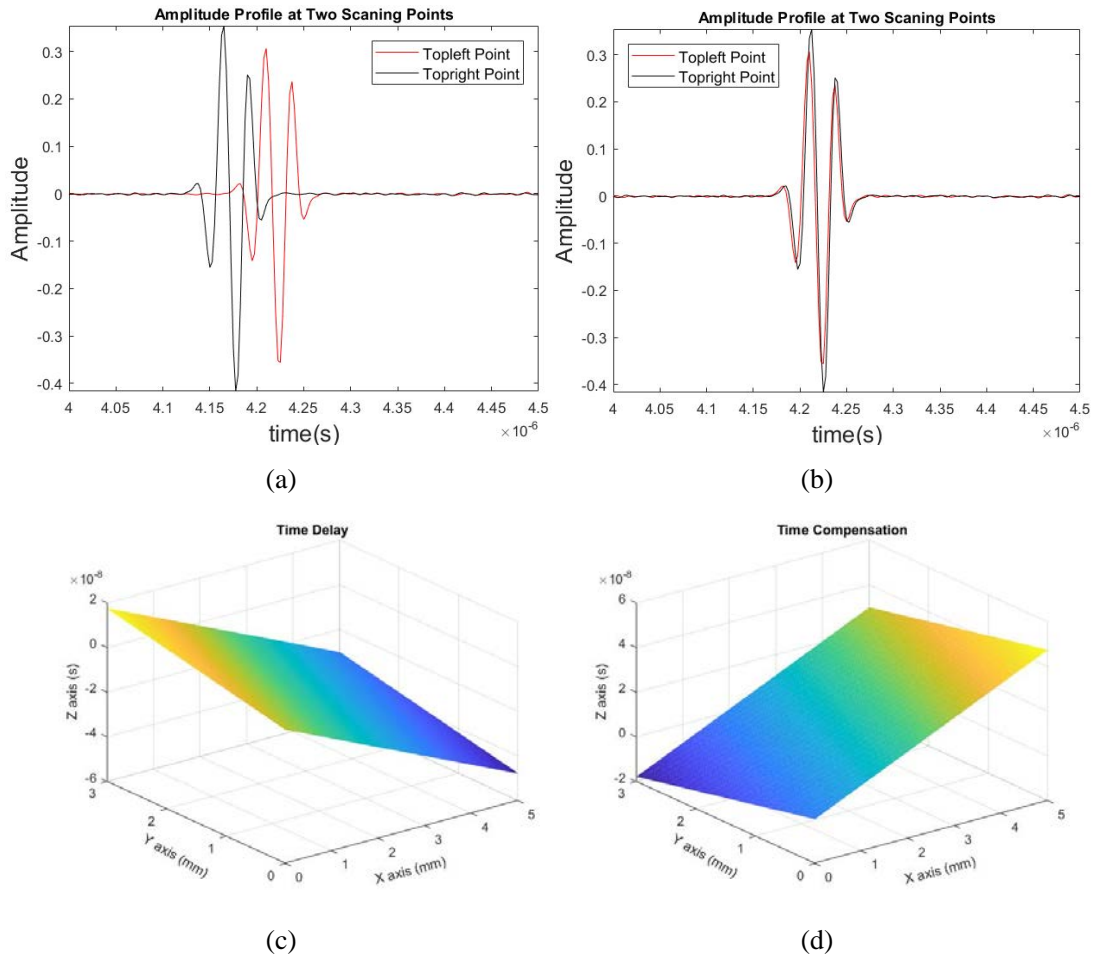


Figure 5.5: Time calibration for case 1. (a) Two signals before calibration. (b) Two signals after calibration. (c) Time delay plane. (d) Time compensation plane.

However, maximum amplitude method and centre of mass method can only work for specific cases which means that they cannot both work well for all cases. This is because of the internal properties of the algorithms. Maximum amplitude method only uses the max amplitude to find pulse location while the centre of mass method takes all the pulse amplitudes into account.

If the time interval of the main reflected part of the pulse is quite narrow compared to the whole pulse duration, maximum amplitude method should be used instead of centre of mass method. Noise would affect the estimation of location seriously in centre of mass method since all the noise is accumulated. Although noise affects the max amplitude value, the location of max amplitude does not shift a lot since the max amplitude is quite large compared to the noise level. Take case 1 as an example, Figure 5.6 shows the results of centre of mass method.

If the time interval of the main reflected part of the pulse is not narrow compared to the whole pulse duration, the centre of mass method should be used instead of the maximum amplitude method. For this kind of pulse, noise could not affect the estimation of location seriously in centre of mass method because the accumulation of noise is quite small compared to the addition of useful reflected pulse amplitude values. Noise affects estimation of pulse location seriously in maximum amplitude method, since the amplitude

profile is relatively flat that even small noise can lead to large shift of location of max amplitude. Take case 4 as an example, Figure 5.7 is used to illustrate the performance of two methods.

Comparing Figure 5.6 and Figures 5.5 (a) (b), we can see that maximum amplitude method works better for case 1. Figure 5.7 shows that centre of mass method works better for case 4. In fact, maximum amplitude method works better for case 1, 2, 3, 5, 6. Centre of mass method works better for case 4, 7 and 8. That is to say, maximum amplitude method works better for systems excited by Ricker signal, and the centre of mass method works better for systems excited by Barker coded signal.

For systems excited by Chirp signal, maximum amplitude works better in case 3 while centre of mass method works better in case 7. Therefore, we cannot say which time calibration method works better for systems excited by Chirp signal. From the theoretical aspect, this is because the time interval of the main reflected part of Chirp signal is neither distinct wide nor narrow.

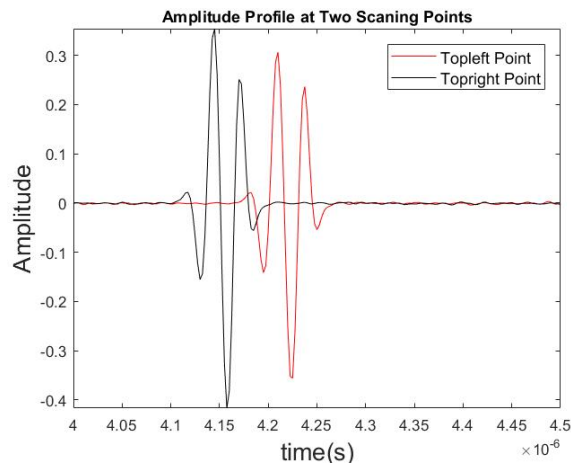


Figure 5.6: Results from center of mass method for case 1

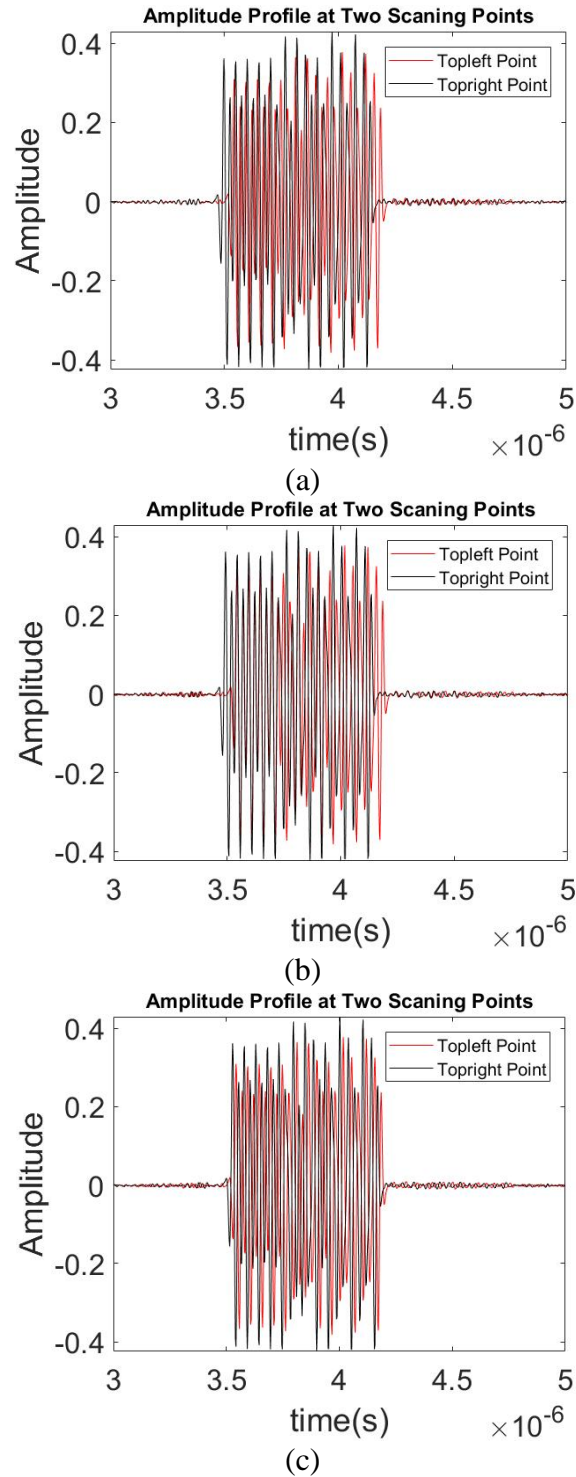


Figure 5.7: Time calibration for case 4. (a) Before calibration. (b) Maximum amplitude method. (c) Centre of mass method.

### 5.3 Discussion on decoding methods

#### 5.3.1 Discussion on filtering domain of Matched filter

Coding is always accompanied by decoding also known as wave compression. After

calibration and interpolation, the received coded signals need to be decoded which is done by filtering with either a Wiener filter or a Matched filter.

The results from performing the filtering in time or frequency domain should be same. Here case 3 is used as an example to prove this for the Matched filter. For case 3, Figure 5.8 shows the filtered signals at two scanning points with excitation signal as matching template. The amplitude of the filtered signal is given in a decibel scale. As shown in Figure 5.8, the filtered signals are so identical that the difference cannot be distinguished by human eyes. However, we expect a slight difference from rounding operation in MATLAB.

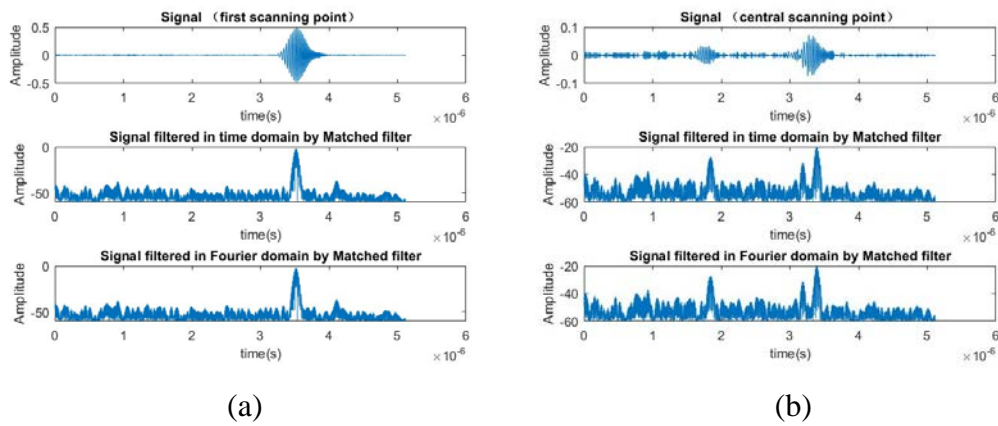


Figure 5.8: Matched filtering both in time and frequency domain. (a) Signals of first scanning point. (b) Signals of central scanning point.

### 5.3.2 Discussion on “noise” parameter of Wiener filter

Both the Match and Wiener filtering are more complicated to implement in the time domain than in the frequency domain due to the involved convolution operation, and also much more time demanding for our 2048 long time samples. The filtering was therefore implemented in the frequency domain using FFT, multiplications, and inverse FFT.

The “noise”  $\lambda$ -parameter in the Wiener filter plays an important role for the filter performance. With case 3 as the example, Figure 5.9 shows signals filtered by the Wiener filters with four different  $\lambda$ -parameters. The signal need to be filtered is collected at first scanning point. Wiener filter is generated from Eq. (3.40). The parameter  $k_c$  is set to 1 and  $\lambda$  is set to 0.1, 1, 500 and 10000 respectively. When  $\lambda$  equals 1 or 0.1, the filtered signals are unusable that the useful information is buried in noise. This is because if  $\lambda$  is too small, the Wiener filter would degenerate to an inverse filter which typically will give division by numbers close to zero for frequencies outside the main band, and a resulting high magnification of the frequency response for these frequencies. When  $\lambda$  equals 500 or 10000, the filtered signals are acceptable. When  $\lambda$  equals 10000, the Wiener filter starts to behave like a Matched filter. Therefore  $\lambda$  is set to 500 to generate a reasonable compromise for the filtered signals. The conclusion is same for other related cases, so  $\lambda$  is set to 500 for all related cases.

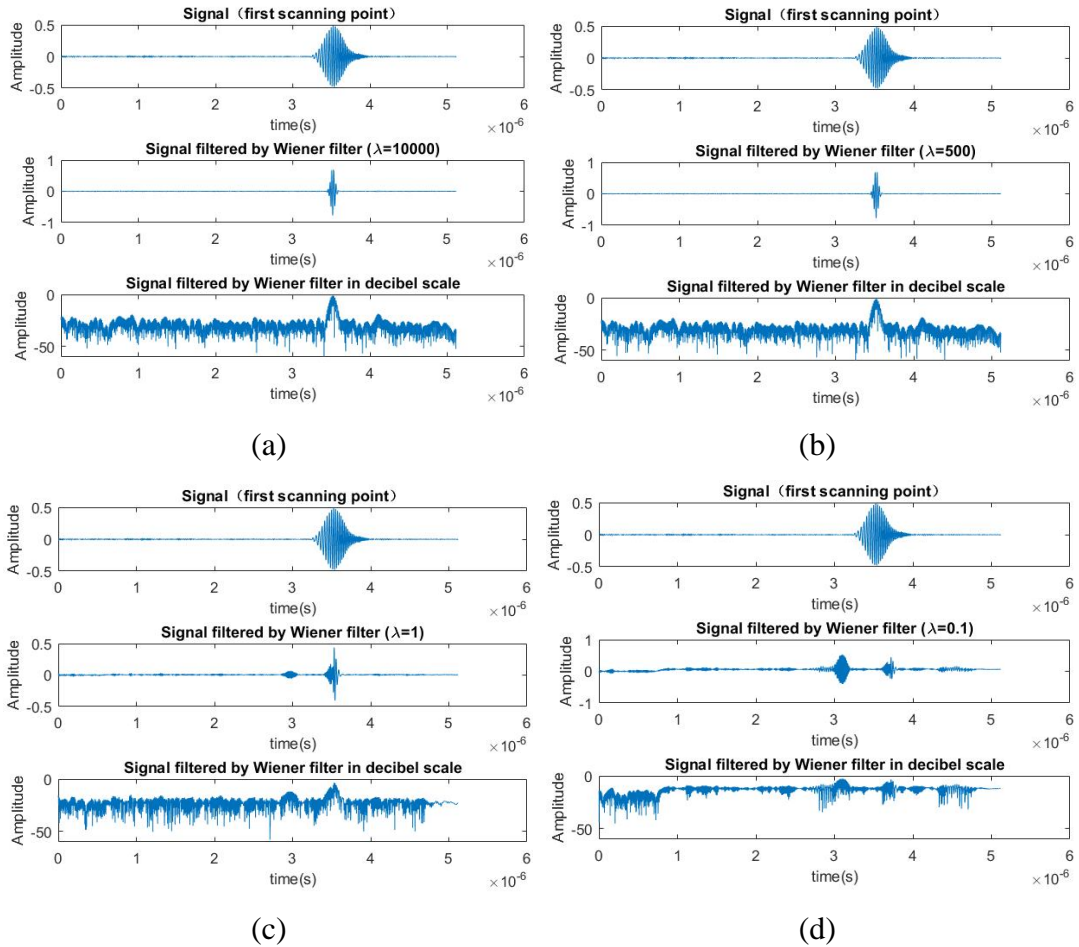


Figure 5.9: Filtered signals of first scanning point. (a)  $\lambda = 10000$ . (b)  $\lambda = 500$ . (c)  $\lambda = 1$ . (d)  $\lambda = 0.1$ .

### 5.3.3 Discussion on SNR, axial resolution and PSL

Important parameters like SNR, axial resolution and PSL can be used to evaluate the performance of decoding methods. The SNR, axial resolution and PSL for all cases are listed in Table 5.1. The average value of SNR at 10 scanning points is used as the value of SNR in the table since it is too complicated to calculate SNR at every scanning points. PSL and axial resolution are calculated in the same way.

The SNR of case 1 is obviously larger than that of case 2. This is because the received signals of case 1 are averaged 16 times while the received signals of case 2 are without averaging. In general, the averaging operation reduces the random noise effectively. The SNR of case 5 is obviously larger than case 6, which is also due to the averaging operation. For all situations of case 3, the SNR does not show much difference regardless of which filter is used. For case 4, the SNR for situations using Wiener filter and Matched filter are almost same if the templates are similar. For all situations in case 7, the SNR does not show much difference regardless of which filter is used. For case 8, SNR of situations using Wiener filter and Matched filter is almost same if the templates are similar.

To summarize, the SNR of situations using coded signals are generally larger than the corresponding situations using no coded signals which points out the advantage of coded ultrasound signals.

Axial resolution and range sidelobe level are more intuitive to evaluate for the performance of the coding and decoding methods. Axial resolution is defined as the mainlobe width which is normally regarded as the distance between the points where their amplitude is half of the peak amplitude. From Table 5.1 we can see that performance of Wiener filter and Matched filter is almost same in terms of resolution. We can also observe that the resolution of coded ultrasound signals is better than the physical resolution. The resolution literally depends on how the mainlobe width is defined. If we use a -20 dB width instead, the resolution of coded ultrasound signals would be worse than the physical resolution.

In terms of range sidelobe level, PSL is used to evaluate it. For all situations of case 3, the difference between maximum and minimum values of PSL is quite small. The same thing happens to case 4, 7 and 8. This means that the filtering method does not really influence PSL. Values of PSL varies greatly between different cases, which means coding method influences PSL much. We also see that values of PSL are lower in case 3 than that of case 4, which suggests that the Chirp coded signal is better than the Barker coded one in terms of sidelobe reduction.

All things considered, Wiener filter and Matched filter all perform well and there is not much difference between them in the aspect of decoding.

<i>Case No.</i>	Excitation	Filter	Template	SNR(dB)	PSL(dB)	Resolution (mm)
1	Ricker pulse	No	No	32.60	--	0.150
2	Ricker pulse	No	No	26.86	--	0.152
3	Chirp signal	Matched filter	Excitation	36.50	-34.81	0.090
3	Chirp signal	Matched filter	Reflection	35.41	-34.27	0.089
3	Chirp signal	Wiener filter	Excitation	36.66	-34.82	0.088
3	Chirp signal	Wiener filter	Reflection	36.61	-34.28	0.089
4	Barker signal	Matched filter	Excitation	31.13	-21.81	0.055
4	Barker signal	Matched filter	Reflection	34.49	-21.35	0.057
4	Barker signal	Wiener filter	Excitation	31.28	-21.76	0.055
4	Barker signal	Wiener filter	Reflection	34.57	-21.36	0.059
5	Ricker pulse	No	No	43.43	--	0.118
6	Ricker pulse	No	No	36.97	--	0.130
7	Chirp signal	Matched filter	Excitation	59.77	-42.56	0.052
7	Chirp signal	Matched filter	Reflection	60.35	-44.60	0.054
7	Chirp signal	Wiener filter	Excitation	61.23	-42.86	0.054
7	Chirp signal	Wiener filter	Reflection	60.99	-44.66	0.054
8	Barker signal	Matched filter	Excitation	55.27	-22.04	0.073
8	Barker signal	Matched filter	Reflection	58.03	-21.04	0.060
8	Barker signal	Wiener filter	Excitation	55.26	-22.49	0.072
8	Barker signal	Wiener filter	Reflection	58.01	-21.72	0.060

Table 5.1: SNR, axial resolution and PSL

### 5.3.4 Discussion on templates

The template will be a decisive factor in the filter performance. In the experiment both the Wiener and Matched filter are generated by reflection signals or coded excitation signals. From the aspect of SNR, axial resolution and PSL we can see that the performance of two different types of template is almost the same. The difference between SNR, resolution and PSL using excitation template and reflection template is quite limited. Sometimes filters generated by excitation template works better while sometimes filters generated by reflection template works better.

## 5.4 Discussion on PZT and PVDF transducers

From Table 5.1 we can see that SNR of signals recorded by PZT transducer is much lower than SNR of signals recorded by PVDF transducer under similar experimental conditions. This indicates that the PVDF transducer tends to yield more robust signals, which is in contradiction to the piezoelectric performance of the materials. Resolution of signals

recorded by PZT transducer and PVDF transducer do not have significant difference under the used conditions which should be comparable. This illustrates that the PVDF transducer has no advantage regarding the axial resolution, although its SNR is better.

The PSL of signals recorded by the PZT transducer is higher than the one from the PVDF transducer when the other experimental conditions are same. This indicates that the PVDF transducer is more capable of yielding a lower noise level, which again is consistent with its higher SNR.

To sum up, the PVDF transducer has shown to perform better than the PZT transducer in the experiment which might be due to the PVDF's material better impedance to water and its higher bandwidth. Another disadvantage with the PZT transducer that we observed in the experiments, is its built-in delay line which probably is needed due to the material's large impedance mismatch with water. The main purpose of this delay line is probably to give sufficient delay to reflection internally in the transducer, so they can be separated from the main pulse using a window function. However, this strategy will not work well for longer waveforms where the multiple reflections evidently introduce unwanted signals, and thereby significantly lower the SNR and increase the PSL [60]. The used silica delay line with a low wave attenuation, also puts an enhanced restriction on the repetition frequency for pulse firing. This is because waves from the previous firing bouncing back and forward inside the delay line, has to die out before the transducer could be fired again. A possibility solution here would be to lower the repetition frequency of pulse firing, with the side-effect of reducing the overall imaging speed.

## 5.5 Discussion on C scan and B scan images

The C scan images based on recorded data with the PZT and PVDF transducers are shown in Figure 5.10 and 5.11, respectively. For Figure 5.10 (b) and (c), and for Figure 5.11 (b) and (c), the excitation signals have been used to generate the filters.

From Figure 5.10 we notice a significant improved SNR for the coded images, which for example makes it possible to observe structures in the middle area of Figures (b) and (c) that are lost in Figure (a) (see the areas indicated with yellow arrows). The images indicate a comparable image quality for the Matched and Wiener method, measured in terms of SNR, dynamic range and contrast. Figure (c) are clearer than Figure (b), this is probably because the Wiener filter can reduce both random noise and speckle noise more efficiently.

The same conclusion can be obtained from Figure 5.11. However, Figures 5.11 (a) (b) and (c) are clearer than Figures 5.10 (a) (b) and (c), respectively. This is because the PVDF transducer tends to produce less noise than the PZT transducer.

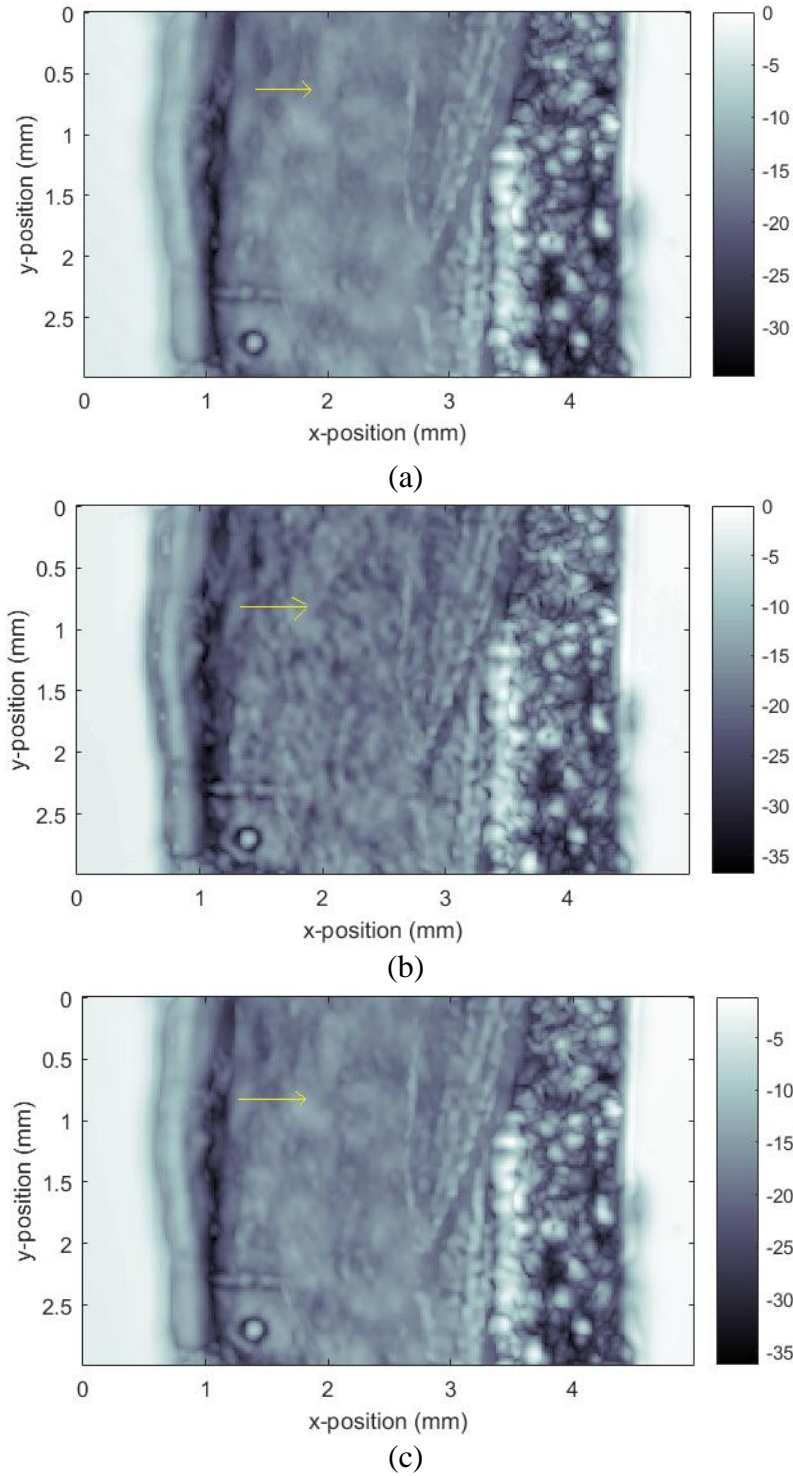


Figure 5.10: C scan images (PZT). Figure (a) is based on Ricker pulse with 16 averaging times, while Figures (b) and (c) have used Chirp wave with a Matched filter and Wiener filter respectively.

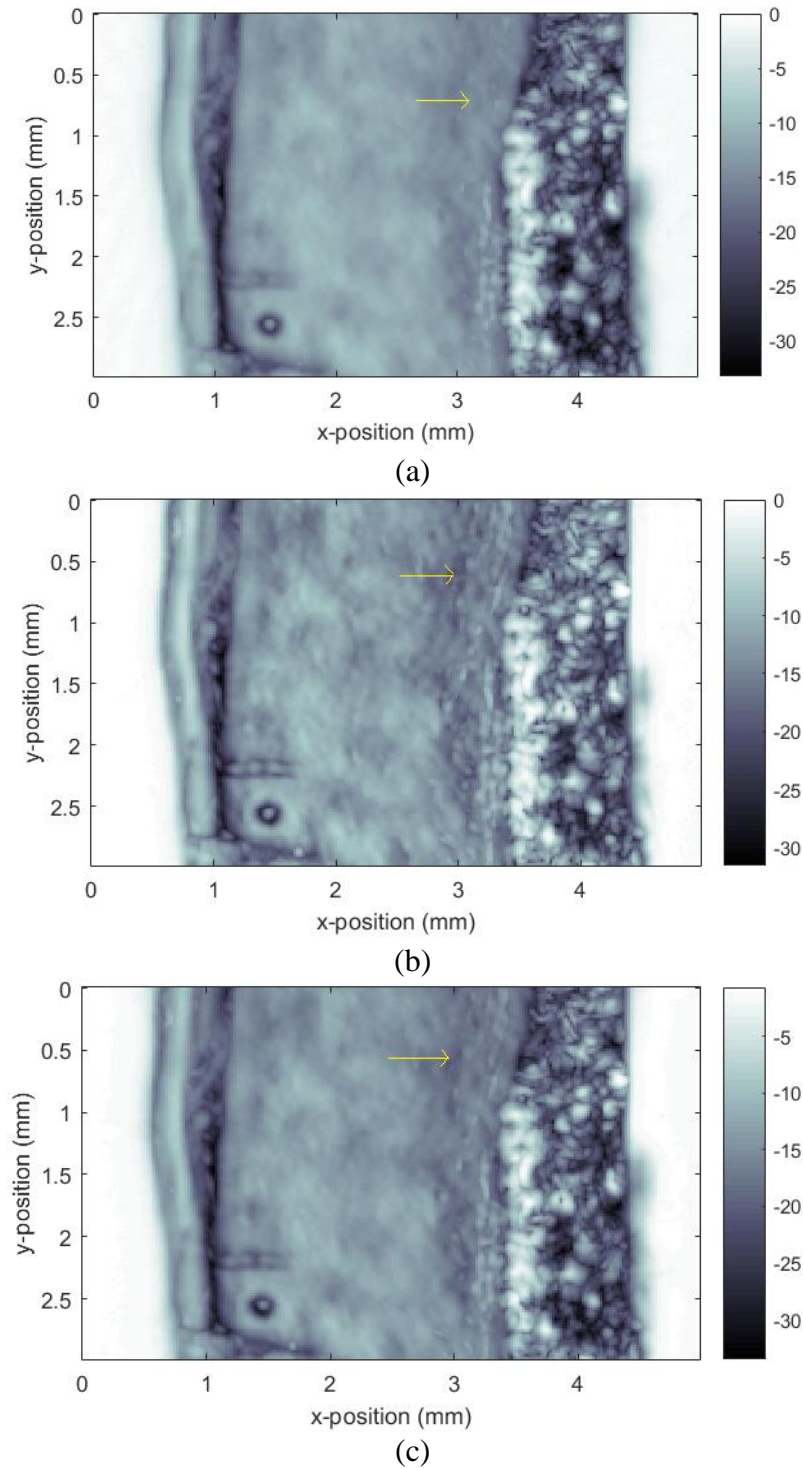


Figure 5.11: C scan images (PVDF). Figure (a) is based on Ricker pulse with 16 averaging times, while Figures (b) and (c) have used Chirp wave with a Matched filter and Wiener filter respectively.

The B scan images based on recorded data generated by the PZT and PVDF transducers are shown in Figure 5.12 and 5.13, respectively. All the B scan images are taken at y-position of 0.5 mm. Figure 5.12 (b) show much more noise than Figure 5.12 (a) because Figure 5.12 (a) is based on received signals with 16 times averaging. Figure 5.12 (d) looks strange while it actually is reasonable. Theoretically the maximum PSL for Barker coded

signal is -22.2 dB, so there are many obvious sidelobes shown in Figure 5.12 (d). For Figure 5.13, the conclusions are same as for Figure 5.12. However, the contrast of B scan images recorded with the PZT transducer is much weaker than for the PVDF transducer, meaning that the noise level of signals recorded by PZT transducer is much higher than that of signals recorded by PVDF transducer. From these B scan images, we clearly notice the presence of the noise for the Ricker pulse. However, this salt-and-pepper noise are highly reduced in the coded images. Some research suggest that Matched filter may produce artificial ringing in the areas with strong backscattering [1]. In the experiment there is not obvious artificial ringing. The conclusions concluded from B scan and C scan images correlated well with conclusions from previous sections.

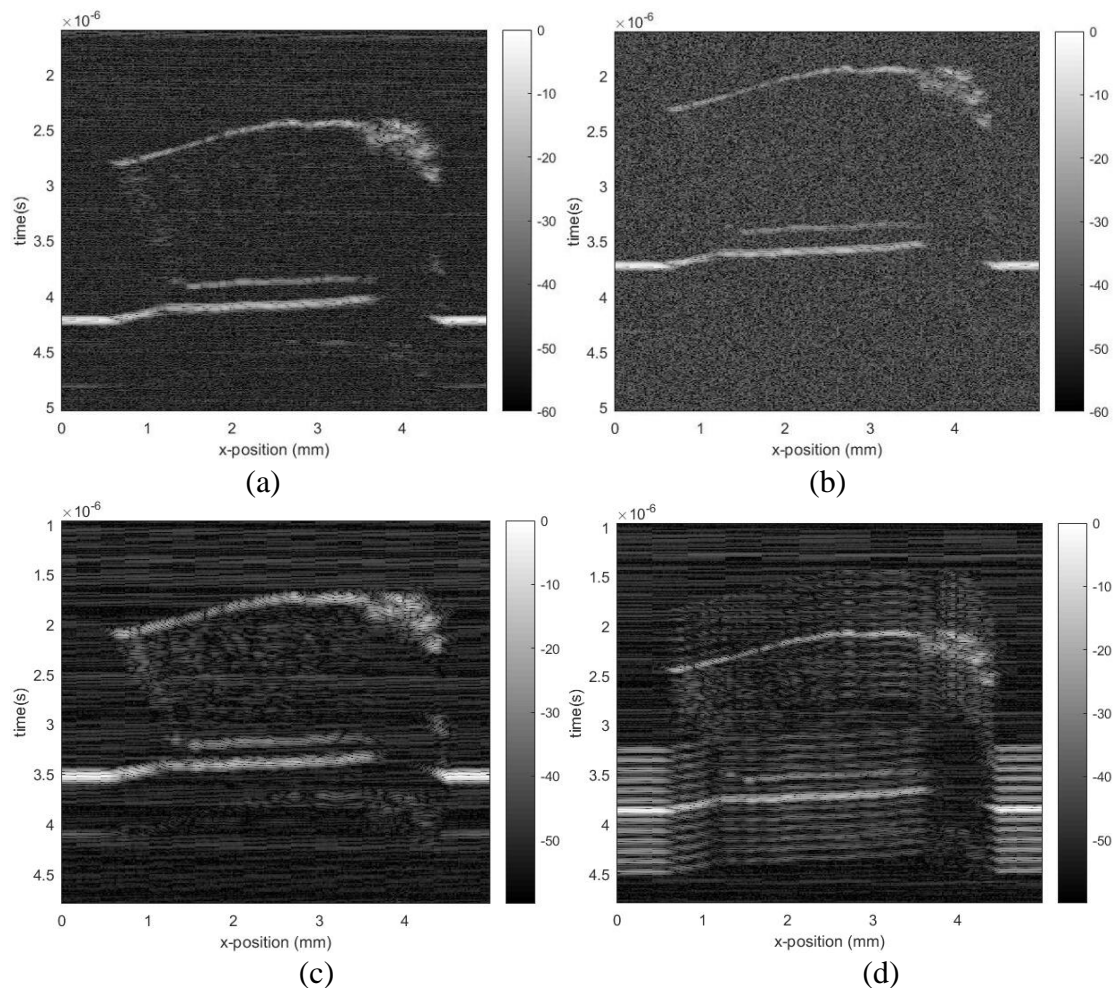


Figure 5.12: B scan images (PZT). Figure (a) based on Ricker pulse with 16 times averaging. Figure (b) based on Ricker pulse without averaging, Figure (c) based on Chirp coded signal and Matched filter, and Figure (d) based on Barker coded signal and Matched filter.

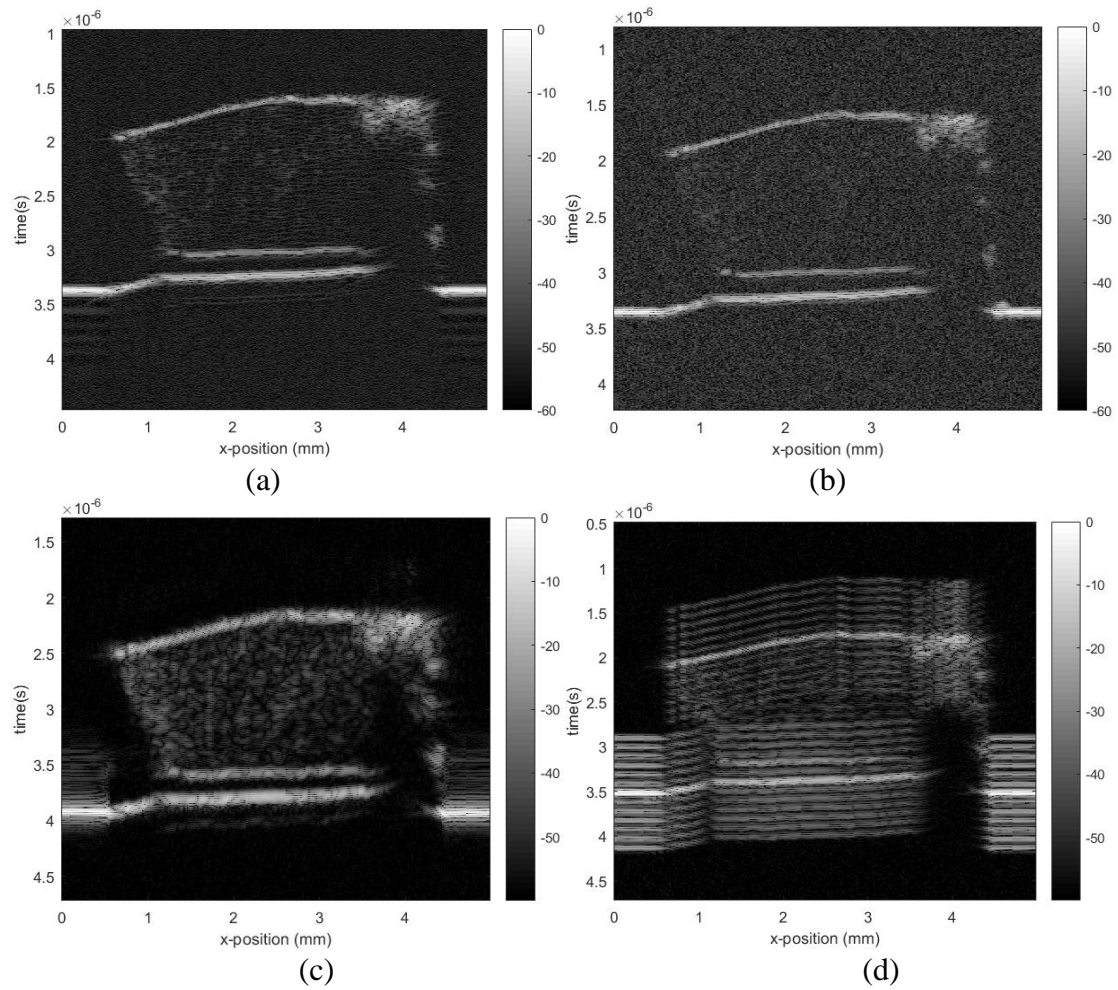


Figure 5.13: B scan images (PVDF). Figure (a) based on Ricker pulse with 16 times averaging. Figure (b) based on Ricker pulse without averaging, Figure (c) based on Chirp coded signal and Matched filter, and Figure (d) based on Barker coded signal and Matched filter.



## Chapter 6

### Main summary, conclusions and further work

This thesis has explored experimentally coded signals used for high frequency ultrasound imaging and related signal processing techniques, with the purpose to enrich efficient coded signals for ultrasound imaging. This chapter presents the main conclusions for the whole thesis and some prospects for possible projects in the next phase.

#### 6.1 Main summary and conclusions

Inspired by coded signals initially used for electromagnetic waves in radars, this thesis describes how coded signals can be transmitted by ultrasonic transducers and subsequently compressed to yield a relatively high SNR without losing axial resolution. Barker and Chirp coded signals were treated theoretically and then implemented experimentally on a SAM platform together with a short Ricker pulse. As a useful target for comparing the three different excitation waves, a sample of articular cartilage was chosen. An important part of the study has also been to compare the Wiener filter and the Matched filter used to compress the coded signals.

One important conclusion of this study is that both Barker and Chirp coded signals favor ultrasound imaging in terms of improved axial resolution, larger SNR yielding larger dynamical range, and reduction of sidelobes. It was also concluded that both the Matched filter and Wiener filter used in the experiment, were capable of providing good compressing of the coded signals. The thesis also compared filter templates based on both the analytical waveform used for the code, and the reflected waveform in the experiment. This investigation showed no significant difference between results whether these filter templates. The performance of two types of transducers was also considered, and it was shown that the PVDF transducer is more conducive to produce high quality images.

#### 6.2 Further work

The proposed work in this thesis could be improved and extended in several aspects. The current study has for instance, considered only two types of coded signals in the thesis, so a further investigation of other types of frequently used codes are desired. This includes for example, Golay codes known to produce small sidelobes. To reduce sidelobes and side effects caused by ultrasonic transducers, pre-distorted coded signals could be added in future projects. There is also a need for extending the proposed calibration method to make it more robust. A limitation with the current experimental study, is also that only one medical sample has been considered. It is therefore a need for exploring the codes and compression methods on other tissue samples, to figure out if the main conclusions given above have a general validity.

In addition to a further experimental testing, it is also suggested to use numerical simulations. It is believed that simulation could give very useful complementary

information. This information should be compared to the experimental results, to give a more comprehensive understanding of for example, physical processes important for the received data and eventually the generated images.

## Bibliography

- [1] Anowarul Habib. In Vitro Volume Imaging of Articular Cartilage Using Chirp-coded High Frequency Ultrasound. *IEEE Ultrasonics Symposium*, 2019.
- [2] Nils Mannicke, Martin Schone. 3-D High-frequency Ultrasound Backscatter Analysis of Human Articular Cartilage. *Ultrasound in Medicine and Biology*. 40(1): 244-257, 2014.
- [3] E. W. van Geffen. IL-37 Diminishes Proteoglycan Loss in Human OA Cartilage: Donor-specific Link Between IL-37 and MMP-3. *Osteoarthritis and Cartilage*. 27(1): 148-157, 2019.
- [4] A. J. Sophia Fox, A. Bedi. The Basic Science of Articular Cartilage: Structure, Composition and Function. *Sports Healthy*. 1(6): 461-468, 2009.
- [5] Sridhar Premkumar. *Text Book of Craniofacial Growth*. Jaypee Brothers Medical Publishers, 2011.
- [6] [www.encyclopedia.com/medicine/anatomy-and-physiology/anatomy-and-physiology/cartilage](http://www.encyclopedia.com/medicine/anatomy-and-physiology/anatomy-and-physiology/cartilage), Webpage, 2019.
- [7] Alan P. Newman. Articular Cartilage Repair. *The American Journal of Sports Medicine*. 26(2): 309-324, 1998.
- [8] A. Matsiko, T. J. Levingstone. Advanced Strategies for Articular Cartilage Defect Repair. *Materials*. 6(2): 637-668, 2013.
- [9] <https://www.news-medical.net/health/What-is-Cartilage.aspx>. Webpage, 2019.
- [10] Temenoff JS, Mikos AG. Review: Tissue Engineering for Regeneration of Articular Cartilage. *Biomaterials*. 21(5): 431-440, 2000.
- [11] Saarakkala S, Waris P, Waris V. Diagnostic Performance of Knee Ultrasonography for Detecting Degenerative Changes of Articular Cartilage. *Osteoarthritis Cartilage*. 20(5): 376–381, 2012.
- [12] Y. Takeuchi. An Investigation of a Spread Energy Method for Medical Ultrasound Systems. *Ultrasonics*. 175-182,1979.
- [13] Vernon L. Newhouse, D. Cathignol. *Introduction to Ultrasonic Pseudo-Random Code Systems*. Springer, 1988.
- [14] M. Pollakowski, H. Ermert. Chirp Signal Matching and Signal Power Optimization in Pulse-Echo Mode Ultrasonic Nondestructive Testing. *IEEE Transactions on Ultrasonics, Ferroelectrics, and Frequency Control*. 41(5): 655-659, 1994.
- [15] M. O' Donnell. Coded Excitation System for Improving the Penetration of Real-Time Phased Array. *IEEE Transactions on Ultrasonics, Ferroelectrics, and Frequency Control*. 39(3): 341-351, 1992.
- [16] T. Misaridis, J. A. Jensen. Use of Modulated Excitation Signals in Medical Ultrasound. Part II: Design and Performance for Medical Imaging Applications. *IEEE Transactions on Ultrasonics, Ferroelectrics, and Frequency Control*. 52(2): 192-207, 2005.
- [17] Chiao R Y, Hao X H. Coded Excitation for Diagnostic Ultrasound: A System Developer's Perspective. *IEEE Transactions on Ultrasonics, Ferroelectrics, and Frequency Control*. 52(2):

- 160-170, 2005.
- [18] B. Haider, P. A. Lewin. Pulse Elongation and Deconvolution Filtering for Medical Ultrasonic Imaging. *IEEE Transactions on Ultrasonics, Ferroelectrics, and Frequency Control*. 45(1): 98-113, 1998.
- [19] Joanne Cowe, John Gittins. Improving Performance of Pulse Compression in a Doppler Ultrasound System Using Amplitude Modulated Chirps and Wiener Filtering. *Ultrasound in Medicine and Biology*. 34(2): 326-333, 2008.
- [20] Vera Behar, Dan Adam. Parameter Optimization of Pulse Compression in Ultrasound Imaging Systems with Coded Excitation. *Ultrasonics*. 42(10): 1101-1109, 2004.
- [21] Barros A. L. P, Machado J. C. A Frequency-Compensated Coded-Excitation Pulse to Improve Axial Resolution of Ultrasonic System. *IEEE Ultrasonics Symposium*. 1651-1654, 2006.
- [22] Thomas L. Szabo. *Diagnostic Ultrasound Imaging: Inside Out*. Elsevier Academic Press, 2014.
- [23] Gonghuan Du. *Fundamentals of Acoustics*. Nanjing University Press, 2012.
- [24] Jinhai Niu. *Principles of Ultrasound and Its Applications*. Shanghai Jiaotong University Press, 2017.
- [25] Richard Haberman. *Applied Partial Differential Equations: With Fourier Series and Boundary Value Problems*. Prentice Hall, 2003.
- [26] Christian Wachinger, Ramtin Shams, Nassir Navab. Estimation of Acoustic Impedance from Multiple Ultrasound Images with Application to Spatial Compounding. *Proceedings on IEEE workshop: Mathematical Methods in Biomedical Image Analysis, Alaska*, 2008.
- [27] Aladin C, Fahrudin S, Dzelaludin J. Application of Ultrasound in Medicine. *Acta Inform Med*. 19(3): 168-171, 2011.
- [28] Otto CM. *Textbook of Clinical Echocardiography*. Elsevier, 2013.
- [29] Viren R. Amin. Ultrasonic Attenuation Estimation for Tissue Characterization. Msc thesis, Iowa State University, 1989.
- [30] Ihor T, Andrzej N. Influence of The Transducer Bandwidth on Compressed Ultrasonic Echoes. *Archives of Acoustics*. 32(4): 903-915, 2007.
- [31] Kapila Epasinghe. Simulation and Visualization of Ultrasound Fields. Msc thesis. University of Oslo, 1997.
- [32] Haifeng W, Wenwu C. Characterization of Ultra-thin Quarter-wavelength Matching Layers of High Frequency Ultrasonic Transducers. *IEEE Ultrasonics Symposium*, 1048-1051, 2003.
- [33] Technical Notes. *Ultrasonic Transducers*. Olympus, 2006.
- [34] G. Andria, F. Attivissimo, N. Giaquinto. Digital Signal Processing Techniques for Accurate Ultrasonic Sensor Measurement. *Measurement*. 30(2): 105-114, 2001.

- [35] D. Marioli, C. Narduzzi. Digital Time-of-Flight Measurement for Ultrasonic Sensors. *IEEE Transactions on Instrumentation and Measurement*. 40(1): 93-97, 1992.
- [36] M. Dell'Isola, M. Canizzo, M. Dritti. Measurement of High Pressure Nature Gas Flow Using Ultrasonic Flowmeters. *Measurement*. 20(2): 75-89, 1997.
- [37] X. Fan. Gearbox Fault Detection Using Hilbert and Wavelet Packet Transform. *Mechanical Systems and Signal Processing*. 20(4): 966-982, 2006.
- [38] M.S Islam, U. Chong. Noise Reduction of Continuous Wave Radar and Pulse Radar Using Matched Filter and Wavelets. *EURASIP Journal on Image and Video Processing*. 1(43), 2014.
- [39] Alexander Ng, Justiaan Swanevelder. Resolution in Ultrasound Imaging. *Continuing Education in Anesthesia Critical Care and Pain*. 11(5): 186-192, 2011.
- [40] Echopedia. [https://www.echopedia.org/wiki/The\\_principle\\_of\\_ultrasound](https://www.echopedia.org/wiki/The_principle_of_ultrasound). web page, 2019.
- [41] Radek Benes, Kamil Riha. Noise Reduction in Medical Ultrasound Images. *Elektrorevue*. 2(3), 2011.
- [42] Are Fritz Charles Jensen. The General Flow-adaptive Filter. Msc thesis. University of Oslo, 2003.
- [43] Jihoon Park, Jin Bum Kang, Jin Ho Chang, Jihoon Park. Speckle Reduction in Ultrasound Imaging. *Biomedical Engineering Letters*. 4(1): 32-40, 2014.
- [44] Carovac A, Smajlovic F, Junuzovic D. Application of Ultrasound in Medicine. *Acta Inform Med*. 19(3): 168-171, 2011.
- [45] Peter Hoskins, Kevin Martin, Abigail Thrush. *Diagnostic Ultrasound: Physics and Equipment*. Cambridge University Press, 2010.
- [46] R. M. Sherekar, A. Pawar. A MATLAB Image Processing Approach for Reconstruction of DICOM Images for Manufacturing of Customized Anatomical Implants by Using Rapid Prototyping. *American Journal of Mechanical Engineering and Automation*. 1(5): 48-53, 2014.
- [47] Zhaohong Zhang. Matched-filter Ultrasonic Sensing: Theory and Implementation. *Texas Instruments*. 2017.
- [48] T. Misaridis, J. A. Jensen. Use of Modulated Excitation Signals in Medical Ultrasound. Part I: Basic Concepts and Expected Benefits. *IEEE Transactions on Ultrasonics, Ferroelectrics, and Frequency Control*. 52(2): 177-191, 2005.
- [49] Coded Excitation System for Improving the Penetration of Real-Time Phased-Array Imaging Systems. *IEEE Transactions on Ultrasonics, Ferroelectrics, and Frequency Control*. 39(3): 341-351, 1992.
- [50] D. R. Wehner. *High-Resolution Radar*. Artech House, 1995.
- [51] Thanassis Misaridis. Ultrasound Imaging Using Coded Signals. PhD thesis. Technical University of Denmark. 2001.
- [52] L. Svilainis. Ultrasonic System Models for the Pulse Trains Excitation Tuning. *Elektronika ir Elektrotechnika*. 22(2): 1392-1215, 2016.
- [53] J. Y. Zhang. The Simulation for Ultrasonic Testing Based on Frequency-Phase Coded Excitation. *8<sup>th</sup> International Conference on Physical and Numerical Simulation of Materials Processing*.

USA, 2016.

- [54] Charles Cook. *Radar Signals: An Introduction to Theory and Application*. Academic Press, 1967.
- [55] T. Misaridis, J. A. Jensen. An Effective Coded Excitation Scheme Based on A Predistorted FM Signal and An Optimized Digital Filter. *IEEE Ultrasonics Symposium*, 1589-1593, 1999.
- [56] R. C. Gonzalez, R. E. Woods. *Digital Image Processing*. Prentice Hall, 2008.
- [57] Frank Melandsø. *Lecture Notes of Ultrasound Imaging Technology*. University of Tromsø. 2018.
- [58] Gradimir V. Milovanovic. *Interpolation Processes: Basic Theory and Applications*. Springer, 2008.
- [59] Andrey A. Samokrutov. *Workshop: Ultrasonic Imaging of Concrete*. Oakland, Canada, 2008.
- [60] Stefan Johann Rupitsch. *Piezoelectric Sensors and Actuators: Fundamentals and Applications*. Springer, 2019.

## **Appendices**





Tel: 781-419-3900  
www.olympus-ims.com

**TRANSDUCER DESCRIPTION**

PART NO.: V3970  
SERIAL NO.: 1188134  
DESIGNATION: 5 IN OLF  
FREQUENCY: 50.00 MHz  
ELEMENT SIZE: 25 in. DIA

**TEST INSTRUMENTATION**

PULSER/RECEIVER: PANMETRICS 5601  
DIGITAL OSCILLOSCOPE: LeCroy LC564A / SN: LC56410253  
TEST PROGRAM: TP103-3  
CABLE: RG-58 AU LENGTH 2FT

**TEST CONDITIONS**

PULSER SETTING: Energy: 1; Damping: 50 Ohm  
RECEIVER SETTING: Gain: 46 dB; Att: 46 dB  
TARGET: 5STEEL BALLS  
JOB CODE: TP200  
WATER PATH: 0.265 in

**MEASUREMENTS PER ASTM E1065**

FOCAL LENGTH --- 0.815 in  
WAVEFORM DURATION:  
-10DB LEVEL -- 0.041 US  
-20DB LEVEL -- 0.045 US  
-40DB LEVEL -- 0.082 US  
SPECTRUM MEASUREMENTS:  
CENTER FREQ. --- 40.04 MHz  
PEAK FREQUENCY -- 40.00 MHz  
-6DB BANDWIDTH -- 80.54 %  
F#: 47.3

**COMMENTS:**

5in STEEL BALL AS EQUAL PHASE REFLECTOR  
1.981 us SILICA DELAY LINE

\*\* ACCEPTED, AUTH. BY:

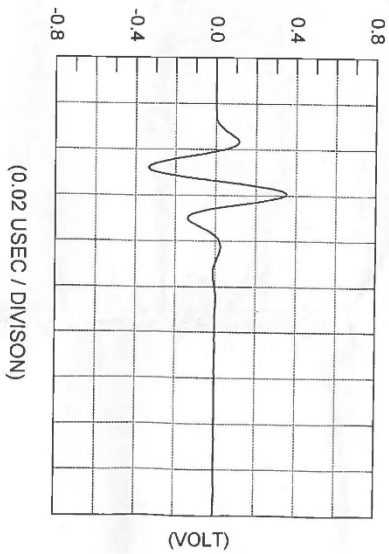
TECHNICIAN ( 7 )

This Certificate may not be reproduced except in full without written approval of OSSA

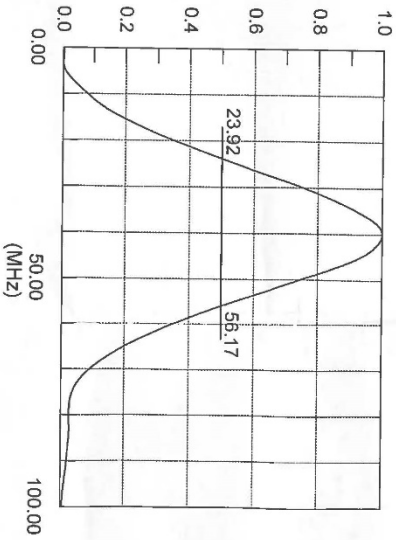
DATE: 01-21-2019

DATE: 01-21-2019

**SIGNAL WAVEFORM**



**FREQUENCY SPECTRUM**







Tel: 781-419-3900  
www.olympus-ims.com

**TRANSDUCER DESCRIPTION**

PART NO.: P175-1-R0.50  
SERIAL NO. 200842  
DESIGNATION: 5 IN OLF  
FREQUENCY: 75.00 MHz  
ELEMENT SIZE: .125 in. DIA.

**TEST INSTRUMENTATION**

PULSER/RECEIVER: PANAMETRICS 6901  
DIGITAL OSCILLOSCOPE: LeCroy LC594A / SN: LC56410293  
TEST PROGRAM: TP103.3  
CABLE: RG 174/U LENGTH: 3FT

**TEST CONDITIONS**

PULSER SETTING: Energy: 1; Damping: 50 Ohm  
RECEIVER SETTING: Gain: 48 DB; Attm: 42 DB  
TARGET: 7/9 STEEL BALLS  
JOB CODE: TP200  
WATER PATH: 0.1111 in

**MEASUREMENTS PER ASTM E1065**

FOCAL LENGTH --- 0.486 in  
WAVEFORM DURATION:  
-14DB LEVEL - 0.024 US  
-20DB LEVEL - 0.043 US  
-40DB LEVEL - 0.099 US  
SPECTRUM MEASUREMENTS:  
CENTER FREQ. --- 49.41 MHz  
PEAK FREQUENCY - 48.60 MHz  
-6DB BANDWIDTH - 75.69 %  
F#: 54.0

**COMMENTS:**

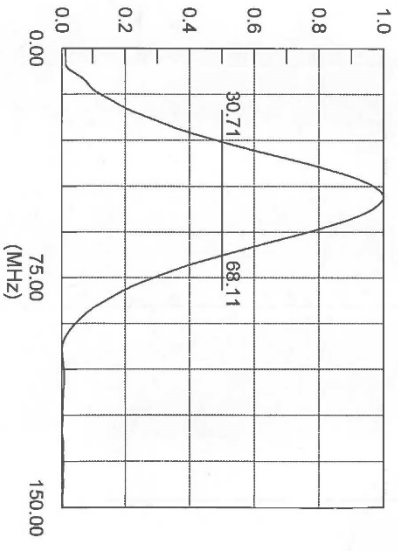
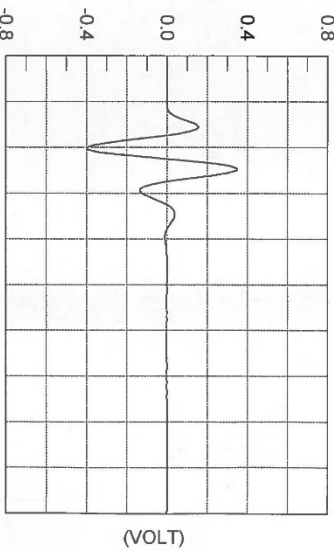
TESTED WITH 6DB AT T/R  
75in STEEL BALL AS EQUAL PHASE REFLECTOR

\*\* ACCEPTED

TECHNICIAN (7)

DATE: 02-25-2017

This Certificate may not be reproduced except in full without written approval of OSSA



TP103 Rev. A

